UNIVERSITÀ DEGLI STUDI DI PARMA

Dottorato di Ricerca in Tecnologie dell'Informazione

XXV Ciclo

NUMERICAL MODELING OF THIN-FILM SOLAR CELLS WITH Cu(In,Ga)Se_2 (CIGS) AND CdTe ABSORBERS

Coordinatore:
Chiar.mo Prof. Marco Locatelli

Tutor:
Chiar.mo Prof. Roberto Menozzi

Dottorando: *Fabrizio Troni*

Gennaio 2013

Ai miei genitori

To my parents

Contents

Introduction 1

1 The numerical model 7

1.1 Frequency domain 10
1.2 Synopsys Sentaurus 11
1.3 The discretization grid 12
1.4 Optics 14

2 Analytical models of the photocurrent 19

2.1 Thin-film solar cell structure 19
2.2 Contribution of the absorber 20
  2.2.1 Quasi-neutral region 20
  2.2.2 Depletion region 24
2.3 Photon flux calculation 25
2.4 Numerical validation 28
2.5 Contribution of the first layers 31
2.6 Summary 36

3 Polycrystalline CIGS 37

3.1 CIGS solar cell numerical modeling 38
3.2 Compact modeling of the dark i-v curve 44
3.3 Numerical simulation of damp heat degradation 51
3.4 Summary 52

4 ZnMgO buffer layer **53**
- 4.1 Numerical model 54
- 4.2 Simulation results 55
  - 4.2.1 ZnMgO thickness and doping 55
  - 4.2.2 Interface states at ZnMgO/CIGS heterostructure 61
- 4.3 Summary 64

5 Modeling of CdTe Solar Cells **65**
- 5.1 Numerical model 66
- 5.2 Simulation results 68
  - 5.2.1 Vertical grain boundaries 68
  - 5.2.2 Horizontal grain boundaries 73
- 5.3 Summary 77

6 Conclusions **79**

A Acronyms **83**

B List of symbols **85**

C Physical constants **87**

Bibliography **89**

Acknowledgements **93**

List of Figures

1 Photovoltaic effect. 2

1.1 Synopsys Sentaurus. 11
1.2 Multibox method used for meshing a square with 0.4 μm *min step*, 0.02 μm *max step*, and 1.5 *ratio* beetwen meshing points. The directions given to the meshing tool are -X and -Y. 13
1.3 Transfer matrix at a generic interface and inside a material for normal incident light. 14

2.1 Basic structure of a CIGS solar cell: (a) window (ZnO), (b) buffer (CdS), (c) absorber (CIGS) 20
2.2 Coordinate system for the quasi-neutral region of the absorber. . . . 21
2.3 Collection of the current generated optically in the quasi-neutral region of the absorber (eq. 2.9) and normalized to its maximum value $q\Phi'$ at the interface with the previous layer. 23
2.4 Coordinate system for the depletion region of the absorber. 24
2.5 Optical waves in a three-layer structure. 26
2.6 Continuous line: optical intensity calculated considering the interference of all layers. Dashed line: optical intensity calculated neglecting the reflected wave b34 in the absorber. 30
2.7 Continuous line: optical generation rate calculated considering the interference of all layers. Dashed line: optical generation rate calculated neglecting the reflected wave b34 in the absorber. 30

2.8 Short circuit current calculated considering the absorber space charge and quasi-neutral terms and adding a constant value of $2.2mA/cm^2$ to take into account the first two layers. The result is obtained for different concentrations of deep states N_b in the absorber as a function of doping. The symbols denote the numerical simulations and the solid lines the compact model developed. 31

2.9 Coordinate system for window and buffer layers. (a) Buffer depletion region; (b) buffer quasi-neutral region; (c) window quasi-neutral region. 32

2.10 Short-circuit current calculated considering all terms. The result is obtained for different concentrations of deep states N_b in the absorber as a function of doping. The symbols denote the numerical simulations and the solid lines the compact model. 36

3.1 Structure of the simulated solar cell. g is the grain size. The region around the GB represents Cu-poor CIGS. 38

3.2 Energy band profile along a horizontal line in the CIGS (see Fig. 3.1). The grain boundary hosts interface donors and is characterized by a valence band offset ΔEV (0.2 eV in this example). 39

3.3 Effect of CIGS grain size on the efficiency, for different values of the GB valence-band discontinuity. 42

3.4 Effect of CIGS grain size on the open circuit voltage, for different values of the GB valence-band discontinuity 42

3.5 Effect of CIGS grain size on the short circuit current, for different values of the GB valence-band discontinuity 43

3.6 Effect of CIGS grain size on the fill factor, for different values of the GB valence-band discontinuity. 43

3.7 Compact model for single-crystal CIGS solar cells. 44

3.8 Dark I-V curves for the single-crystal cell (no GBs), with different bulk defect densities N_B (10^{12}, 10^{13}, 10^{14}, 10^{15}, 10^{16} cm^{-3}) . The dots are numerical simulation results, the solid lines are obtained with the two-diode compact model. 45

3.9 Two-diode compact model parameters J_{01} (circles) and J_{02} (squares) for the fit of Fig. 3.8, as a function of bulk trap density. 46

3.10 Electron and hole current density map for a cell with $N_I = 2{\cdot}10^{12}$ cm^{-2} defects at the grain boundary and $N_B = 10^{14}$ cm^{-3} in the grain interior. $\Delta EV = 0$. $V_D = 0.8$ V. 47

3.11 Solid line: dark current characteristics for a cell with $N_I = 2{\cdot}10^{12} cm^{-2}$ defects at the grain boundary, $\Delta EV = 0$, and $N_B = 10^{14}$ cm^{-3}. Dots: electron current flowing outside the GB just below the CdS/CIGS interface. Dashed line: electron current flowing along the GB just below the CdS/CIGS interface. 48

3.12 Compact model for polycrystalline CIGS solar cells. 49

3.13 Dark current characteristics for a cell with $N_I = 2{\cdot}10^{12} cm^{-2}$ defects at the grain boundary; $\Delta EV = 0$; $N_B = 10^{14}$, 10^{15}, 10^{16} cm^{-3}. Solid line: numerical simulation. Dots: 4-diode compact model. 49

3.14 Dark current characteristics for a cell with $N_I = 2{\cdot}10^{11}$, $4{\cdot}10^{11}$, $2{\cdot}10^{12}$, $4{\cdot}10^{12}$ cm^{-2} defects at the grain boundary; $\Delta EV = 0$; $N_B = 10^{14}$ cm^{-3}. Solid line: numerical simulation. Dots: 4-diode compact model. . . 50

3.15 Four-diode compact model parameters J_{03} (circles) and J_{04} (squares) for the fit of Fig. 3.14, as a function of GB trap density. 50

3.16 Pre- and post-stress defect distribution in the bulk of the CIGS absorber for the simulation of damp heat degradation ([20]). 52

4.1 Cell reflectivity vs. window layer thickness. 55

4.2 Band diagram for the $Zn_{1-x}Mg_xO$/CIGS interface. $x = 0.36$, $t_W = 80$ nm. The arrow indicates increasing values of n_W: 10^{12}, 10^{16}, 10^{17}, 10^{18} cm^{-3}. 56

4.3 Short-circuit current vs. $Zn_{1-x}Mg_xO$ thickness for $x = 0.36$, and for two values of n_W, the electron concentration in the $Zn_{1-x}Mg_xO$. . . 57

4.4 Open circuit voltage vs. $Zn_{1-x}Mg_xO$ thickness for $x = 0.36$, and for two values of n_W, the electron concentration in the $Zn_{1-x}Mg_xO$. . . 57

4.5 Cell efficiency vs. $Zn_{1-x}Mg_xO$ thickness for x = 0.36, and for two values of n_W, the electron concentration in the $Zn_{1-x}Mg_xO$. 58

4.6 Short-circuit current vs. $Zn_{1-x}Mg_xO$ thickness for x = 0.19, and for two values of n_W, the electron concentration in the $Zn_{1-x}Mg_xO$. . . 59

4.7 Cell efficiency vs. $Zn_{1-x}Mg_xO$ thickness for x = 0.19, and for two values of n_W, the electron concentration in the $Zn_{1-x}Mg_xO$. 59

4.8 Cell efficiency vs. $Zn_{1-x}Mg_xO$ electron concentration. 60

4.9 Band diagram for the $Zn_{1-x}Mg_xO$/CIGS interface. x = 0.19, t_W = 80 nm. The arrow indicates increasing values of n_W: 10^{12}, 10^{16}, 10^{17}, 10^{18} cm^{-3}. 60

4.10 Short-circuit current vs $Zn_{1-x}Mg_xO$ electron concentration. x = 0.19. N_{IT}= 10^{11} cm^{-2} (squares), N_{IT}= 10^{12} cm^{-2} (circles), N_{IT}= 10^{13} cm^{-2} (triangles). 62

4.11 Open circuit voltage vs $Zn_{1-x}Mg_xO$ electron concentration. x = 0.19. N_{IT}= 10^{11} cm^{-2} (squares), N_{IT}= 10^{12} cm^{-2} (circles), N_{IT}= 10^{13} cm^{-2} (triangles). 62

4.12 Fill factor vs $Zn_{1-x}Mg_xO$ electron concentration. x = 0.19. N_{IT}= 10^{11} cm^{-2} (squares), N_{IT}= 10^{12} cm^{-2} (circles), N_{IT}= 10^{13} cm^{-2} (triangles). 63

4.13 Cell efficiency vs $Zn_{1-x}Mg_xO$ electron concentration. x = 0.19. N_{IT}= 10^{11} cm^{-2} (squares), N_{IT}= 10^{12} cm^{-2} (circles), N_{IT}= 10^{13} cm^{-2} (triangles). 63

5.1 Schematic structure of the simulated CdTe solar cell. a) Model with charged vertical and horizontal grain boundaries. b) Partial model considering only a vertical neutral grain boundary. 67

5.2 Impact of the grain size g (in the structure of Fig .5.1b) on the solar cell conversion efficiency η for different values of the CdTe doping density N_A. 69

5.3 Impact of the grain size g (in the structure of Fig. 5.1b) on the solar cell open circuit voltage V_{OC} for different values of the CdTe doping density N_A. 69

5.4 Impact of the grain size g (in the structure of Fig .5.1b) on the solar cell short circuit current J_{SC} for different values of the CdTe doping density N_A. 70
5.5 Impact of the grain size g (in the structure of Fig .5.1b) on the solar cell fill factor FF for different values of the CdTe doping density N_A. 70
5.6 Surface recombination rate integrated along the grain boundary as a function of the density of Cl_{Te} states. $N_A = 7 \cdot 10^{15}$ cm^{-3}. 71
5.7 Band diagram near the (vertical) grain boundary, for different values of the density of Cl_{Te} states at the grain boundary. $N_A = 7 \cdot 10^{15}$ cm^{-3}. 72
5.8 Vertical current distribution along a horizontal cut near the metallurgical junction in the presence of a vertical grain boundary, for different values of the density of Cl_{Te} states at the grain boundary (see Fig. 5.7). $N_A = 7 \cdot 10^{15}$ cm^{-3}. 72
5.9 Hole current density map for the solar cell operating at its maximum power point (anode-cathode voltage: 0.675 V). The structure is composed by six grains: grain boundaries are indicated by dashed lines. The density of Cl_{Te} states at every grain boundary is $N_{GB} = 5 \cdot 10^{11}$ cm^{-2}, while the doping density of the CdTe is $N_A = 7 \cdot 10^{15}$ cm^{-3}. . 74
5.10 Band diagram along a vertical cut at lateral position = 5 μm in the structure in Fig. 5.9. Solid lines: maximum power point; dashed lines: thermal equilibrium. 74
5.11 Hole concentration along a vertical cut at lateral position = 5 μm in the structure in Fig. 5.9. Solid line: maximum power point; dashed line: thermal equilibrium. 76
5.12 Hole concentration along a horizontal cut at depth = 2.5 μm (i.e., along the horizontal grain boundaries) in the structure in Fig 5.9. Solid line: maximum power point; dashed line: thermal equilibrium. 76

List of Tables

2.1 Trap parameters for the validation of the analytical model of the photocurrent. 28

2.2 Material parameters for the validation of the photocurrent analytical model. 29

3.1 Polycrystalline CIGS material parameters. 40

3.2 Damp heat simulation results. 51

4.1 $Zn_{1-x}Mg_xO$/CIGS interface trap parameters. 61

5.1 CdTe material parameters. 66

5.2 CdTe solar cell performance. a) Single-crystal, N_A = 7·10^{15} cm^{-3}. b) Columnar poly-crystalline cell (vertical grain boundaries only), g = 1 μm, no Cl_{Te} states, N_A = 2·10^{14} cm^{-3}. c) Columnar poly-crystalline cell (vertical grain boundaries only), g = 1 μm, no Cl_{Te} states, N_A = 7· 10^{15} cm^{-3}. d) Columnar poly-crystalline cell (vertical grain boundaries only), g = 1 μm, N_{GB} = 5·10^{11} cm^{-2}, N_A = 7· 10^{15} cm^{-3}. e) Columnar polycrystalline cell (vertical grain boundaries only), g = 5 μm, no Cl_{Te} states, N_A = 7· 10^{15} cm^{-3}. f) Columnar polycrystalline cell (vertical grain boundaries only), g = 5 μm, N_{GB} = 5·10^{11} cm^{-2}, N_A = 7· 10^{15} cm^{-3}. g) Vertical and horizontal GBs (structure of Fig. 5.9), N_{GB} = 5·10^{11} cm^{-2}, N_A = 7 · 10 ^{15} cm $^{-3}$. 75

Introduction

In the last three centuries we learned how to harness increasing amounts of energy to satisfy our needs. We farm, move, light, save lives, build, communicate, do most of everyday actions using technologies empowered by the energy we extract from our planet. This change happened in a very short time compared to every biological cycle, and to preserve what we know as the *modern world*, we must use renewable energy sources and balance our energetical needs with the ecosystem. Traditional examples of renewable energy are wind and water, used by windmills and watermills since a long time. This mechanical energy comes from the Sun, which heats the atmosphere and evaporates the water, creating winds and running the water cycle.
In 1839 Edmond Becquerel discovered the photoelectric effect and in the 1950s the first silicon solar cell was produced with a conversion efficiency of 6%. Starting from very expensive military and space applications, solar cells have become more and more popular and cheap and are now competitive with fossil fuels.

Electricity is the most flexible form of energy but also the most expensive to produce. The actual scenario is very favourable to the use of energy in this form. Electrical motors are light, efficient and they do not pollute when they are used. Without the emission of harmful fumes we can move (many countries are investing into electrical transportation), air-condition (heat pumps allow to move heat from indoor to outdoor and vice versa) and satisfy most of our needs efficiently. The question about this evolution we are living is: how can we produce electricity without creating pollution?
There are different ways to obtain clean electricity; this work studies thin-film solar cells for the photovoltaic conversion of sunlight. This technology has a huge potential

and relies on the most common and abundant source of energy: the Sun. Everywhere there is life there is sunlight: even where there is no connection to the electrical grid or where traditional methods are not convenient this technology promises to satisfy the local energy needs.

A basic explanation of the photovoltaic effect and how it is used in solar cells is given in Fig. 1. When a semiconductor absorbs a photon with energy greater than the bandgap, an electron is excited from the valence band to the conduction band leaving a hole behind. This generated electron-hole pair is free to move when an external force is applied. In a solar cell this force is mainly due to the electric field originated from the pn junction built-in potential. This basic principle combines with several other mechanisms, e.g. diffusion and recombination, to determine the output of the solar cell. The goal is to collect the photogenerated carriers efficiently using electrical contacts and let them flow through an external circuit to obtain electrical power.

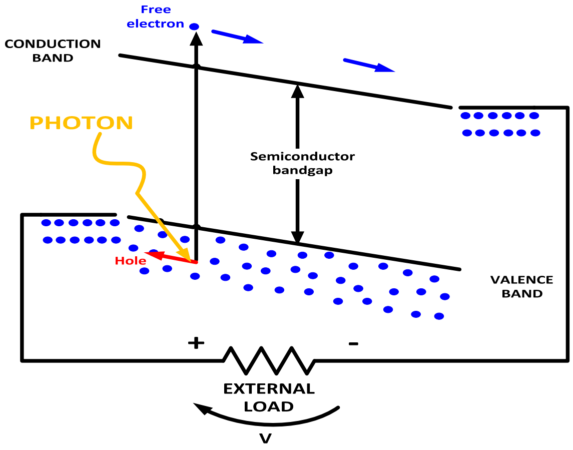

Figure 1: Photovoltaic effect.

The electricity produced using photovoltaics is classified among the "renewable energies", meaning that we are introducing a cycle that can last for an indefinite time. From this perspective one of the critical features of a renewable energy plant is the ability to produce more energy than the amount spent to build it. If we consider tradi-

tional single-crystalline silicon solar cells, five to ten years are needed to obtain back the initial energy investment, while for thin-film technologies this energy payback time drops to few years. While, due to overproduction and worldwide commercial crisis, the market is still dominated by the traditional single- and poly-crystalline silicon, the price to produce a thin-film solar cell is lower and these technologies are very promising under various perspectives. Only the use of a thin-film allows choosing a large variety of substrates and growing the solar cell on many different materials, including flexible polymers and materials used in construction like ceramics or steel.
This thesis analyses the world of thin-film solar cells focusing on two kind of technologies, the first based on copper-indium-gallium diselenide, also called CIGS, the second one on cadmium telluride.

The aim of this work in particular is giving suggestions on how to increase the conversion efficiency of these devices by improving knowledge and understanding of their physical behavior.

Thin-film solar cells based on CIGS or CdTe absorbers have been studied in research laboratories for at least 20 years, but only recently entered the phase of industrial production. While still lagging behind their Si-based competitors in terms of efficiency and dollars/Watt, these technologies are poised to conquer increasing market shares, and perhaps even market dominance. Thin-film solar cells based on Cu(In,Ga)Se2 (CIGS) show record efficiencies among thin-film technologies, with manufacturers introducing mass production processes yielding cells with efficiencies in the 13-15% range [1]. Lab specimens can provide power conversion efficiency as high as 20% [2], despite the poly-crystalline structure of the semiconductor thin film. Several papers were published on material growth, processing and characterization on one side, and on the performance of finished cells and modules on the other, but there is still a gap to fill in between: some of the specific features of CIGS cells, specifically those pertaining to the behavior of grain boundaries and hetero-junctions, are still under debate, and a complete understanding of the relationship between material characteristics and cell behavior is not available yet.
Thin-film solar cells based on CdTe still underperform compared with theoretical limits and even with CIGS cells [3], and in spite of a relatively long history of re-

search and development, there is still room and need for better understanding of the physics underpinning the photovoltaic performance of CdTe cells and modules.

One difficulty lies in the fact that while single crystal materials used in traditional (silicon) and high efficiency tandem (GaAs-based) solar cells are well-known and fully characterized, poly-crystalline materials used in thin-film solar cells show widely varying characteristics depending on growth/deposition process and conditions; the poly-crystalline nature of the absorber is itself an obstacle along the path to full understanding of the cell behavior, and often the device is studied by simulating an equivalent single-crystal solar cell where the material parameters, such as carrier lifetimes, are modified to give a reasonable match of the experiments. This approach has the major advantage of allowing a one-dimensional description of the cell, and the use of efficient and widespread one-dimensional simulation tools like SCAPS [4]. However, the actual current transport mechanisms, which are necessarily affected by the presence of grain boundaries, cannot be investigated using this approximation; consequently, this aspect of device design and optimization is neglected.

Chapther 1 provides the basic concepts and equations of the numerical model used in this thesis, explaining the electrical and optical problem. An overview of the simulation suite Synopsys Sentaurus introduces the main software used to the reader.

The second chapter develops an analytical model of the photocurrent of a thin film solar cell. This study is related to CIGS thin-film solar cell and validated for this technology; however, its validity and significance embrace most of the thin-film technologies. The model rewrites classical equations into the context of thin-film solar cells, providing a detailed derivation of the equations governing each region.

Chapter 3 deals with the polycrystalline structure of CIGS. The presence of defect-rich grain boundaries with possible band-gap modifications is a specific feature of these cells taken into account in this model. Besides studying these cells with two-dimensional numerical simulations, this chapter develops an analytical model of the dark I-V characteristics. While the single-crystal structure behavior will be accurately described by a standard two-diode model, a four-diode model is necessary to describe the effect of active grain boundaries. The only parameters of these two models are the diode saturation currents, leading to a two-parameter and a four-parameter

model, respectively.
Finally, a few simulations address the topic of cell degradation under damp heat stress conditions.

Chapter 4 examines the use of ZnMgO as a replacement of toxic CdS in the standard structure ZnO/CdS/CIGS. In this respect, ZnMgO has proven to be a suitable replacement for CdS, due to its wide bandgap (i.e., low absorption) and convenient band alignment with the CIGS absorber. This chapter provides theoretical indications regarding $Zn_{1-x}Mg_xO$ bandgap (i.e., different Mg content x), thickness, and conductivity, with and without defects at the $Zn_{1-x}Mg_xO$/CIGS interface.

Chapter 5 develops a two-dimensional numerical model of a CdTe solar cell, considering grain boundaries and their effect on current transport. The impact of recombination at vertical grain boundaries (GBs) as a function of CdTe grain size and doping is analyzed as a starting point. This case considers a columnar structure for the CdTe grains with charge-neutral grain boundaries. In a second set of simulations, the presence of the Cl_{Te} states is considered. The model is extended to consider different grain orientation and current transport through GBs. Change of GB resistivity under illumination and bi-dimensional current transport are modeled and discussed in this chapter.

Chapter 1

The numerical model

This work is based on the simulation of physics-based models created with the commercial software Synopsys Sentaurus [5, 6]. The influence of material parameters on device characteristics is explained through the solution of partial differential equations subject to specific boundary conditions and compact analytical modelling. While numerical models provide a more accurate information, analytical models help a better understanding. This chapter explains the basic concepts of the numerical model and its main equations.

The electrostatics is described by the Poisson equation:

$$\nabla \cdot (\varepsilon_r \varepsilon_0 \nabla \Psi) = q(p - n + N_D - N_A) - \rho_T \tag{1.1}$$

where $\varepsilon_r \varepsilon_0$ is the dielectric constant, Ψ is the electrostatic potential, p and n are the free carrier concentrations, N_D and N_A are the density of donor and acceptor doping levels, ρ_T is the charge of the additional trap states.

This equation is solved together with the continuity equations, which assume the following form in the steady-state condition:

$$\nabla \cdot \overrightarrow{J_n} = -\nabla \cdot \overrightarrow{J_p} = q(R - G) \tag{1.2}$$

where J_n and J_p are the electron and hole current densities, R is the recombination rate, and G is the generation rate.
The recombination through states inside the band gap of the semiconductor follows the non-radiative Shockley-Read-Hall model:

$$R = \frac{N_0 v_{TH}^n v_{TH}^p \sigma_n \sigma_p (np - n_i^2)}{v_{th}^n \sigma_n (n + n_1) + v_{th}^p \sigma_p (p + p_1)} \tag{1.3}$$

with

$$n_1 = n_i \cdot e^{\frac{E_T}{kT}} \qquad p_1 = n_i \cdot e^{\frac{-E_T}{kT}} \tag{1.4}$$

$$v_{TH}^{n,p} = \sqrt{\frac{3kT}{m_{n,p}}} \tag{1.5}$$

where N_0 is the density of states of the considered level, v_{TH}^n and v_{TH}^p are the electron and hole thermal velocities, σ_n and σ_p are the capture cross section of the trap centre for electrons and holes, n and p are the free carrier concentrations, n_i is the intrinsic density, E_T is the energy level, k is the Boltzmann constant, m_n and m_p are effective masses, and T is the temperature.
The occupation probability of a state at energy E is given by the Fermi-Dirac statistic:

$$f(E) = \frac{1}{1 + e^{\frac{E - E_F}{kT}}} \tag{1.6}$$

where E_F if the Fermi energy.
In low field regime the mobility μ and the diffusivity D are proportional and given by the Einstein relation:

$$D_n = \frac{kT}{q} \mu_n \qquad D_p = \frac{kT}{q} \mu_p \tag{1.7}$$

When 1.7 holds, the current equations take the form:

$$\overrightarrow{J_n} = n\mu_n \nabla E_{Fn} \qquad \overrightarrow{J_p} = p\mu_n \nabla E_{Fp} \tag{1.8}$$

where E_{Fp} and E_{Fp} are the quasi-Fermi levels.
For a non-degenerate semiconductor they are associated to the carrier desities by

$$n = N_C(x)e^{\frac{E_{Fn}-E_C}{kT}} \qquad p = N_V(x)e^{\frac{E_V-E_{Fp}}{kT}} \tag{1.9}$$

where N_C and N_V are the effective densities of states in the conduction and valence band, E_C and E_V are the conduction and valence band edges.
Equations 1.9 can be written in the form:

$$E_{Fn} = E_C + kTlog\left(\frac{n}{N_C}\right) \qquad E_{Fp} = E_V - kTlog\left(\frac{p}{N_V}\right) \tag{1.10}$$

The spatial derivatives of 1.10 assume the form:

$$\begin{aligned} \frac{dE_{Fn}}{dx} &= \frac{dE_C}{dx} + kT\left[\frac{1}{n}\frac{dn}{dx} - \frac{1}{N_C}\frac{dN_C}{dx}\right] \\ \frac{dE_{Fp}}{dx} &= \frac{dE_V}{dx} - kT\left[\frac{1}{p}\frac{dp}{dx} - \frac{1}{N_V}\frac{dN_V}{dx}\right] \end{aligned} \tag{1.11}$$

The band edges E_C and E_V are related to the electron affinity χ, the band gap E_G and the applied voltage V by:

$$\begin{aligned} E_C(x) &= E_0 - \chi(x) - qV(x) \\ E_V(x) &= E_0 - \chi(x) - E_G(x) - qV(x) \end{aligned} \tag{1.12}$$

where E_0 is the vacuum reference level.

Combining Eq.1.11 with Eq.1.12 we obtain the current expressions for an heterojunction:

$$\begin{aligned} J_n(x) &= -nq\mu_n\left[\frac{d}{dx}\left(V+\frac{\chi(x)}{q}\right)-\frac{kT}{qN_C}\frac{dN_C}{dx}\right]+qD_n\frac{dn}{dx} \\ J_p(x) &= -pq\mu_p\left[\frac{d}{dx}\left(V+\frac{\chi(x)+E_G(x)}{q}\right)+\frac{kT}{qN_V}\frac{dN_V}{dx}\right]-qD_p\frac{dp}{dx} \end{aligned} \tag{1.13}$$

In addition to carrier drift due to the electric field $-dV/dx$ and diffusion due to the carrier density gradient, eqs. 1.13 have terms taking into account compositional variation, spatial dependence of electron affinity, variation of band gap and density of states in the bands.

1.1 Frequency domain

The simulation of frequency response breaks the steady-state condition and time derivative appears in the continuity equation. The system describing the device physics becomes:

$$\begin{cases} \nabla\cdot(\varepsilon_r\varepsilon_0\nabla\Psi)+q(p-n+N_D-N_A)+\rho_T=0 \\ \nabla\cdot\overrightarrow{J_n}-q(R-G)-q\frac{\delta n}{\delta t}=0 \\ \nabla\cdot\overrightarrow{J_p}+q(R-G)+q\frac{\delta n}{\delta t}=0 \end{cases} \tag{1.14}$$

Using the notation:

$$\begin{cases} F_\Psi(\Psi,n,p)=\nabla\cdot(\varepsilon_r\varepsilon_0\nabla\Psi)+q(p-n+N_D-N_A)+\rho_T \\ F_n=\nabla\cdot\overrightarrow{J_n}-q(R-G); \qquad \dot{G}_n=q\frac{\delta n}{\delta t} \\ F_p=\nabla\cdot\overrightarrow{J_p}+q(R-G); \qquad \dot{G}_p=q\frac{\delta n}{\delta t} \end{cases} \tag{1.15}$$

and using the first order terms of the Taylor's series around the DC operating point, we can write the small-signal approximation of the system 1.14:

$$\begin{cases} \left.\frac{\delta F_\Psi}{\delta \Psi}\right|_{DC}\tilde{\Psi} + \left.\frac{\delta F_\Psi}{\delta n}\right|_{DC}\tilde{n} + \left.\frac{\delta F_\Psi}{\delta p}\right|_{DC}\tilde{p} = 0 \\ \left.\frac{\delta F_n}{\delta \Psi}\tilde{\Psi}\right|_{DC} + \left.\left(\frac{\delta F_n}{\delta n} - i\omega\frac{\delta G_n}{\delta n}\right)\right|_{DC}\tilde{n} + \left.\frac{\delta F_n}{\delta p}\right|_{DC}\tilde{p} = 0 \\ \left.\frac{\delta F_p}{\delta \Psi}\tilde{\Psi}\right|_{DC} + \left.\frac{\delta F_p}{\delta n}\right|_{DC}\tilde{n} + \left.\left(\frac{\delta F_p}{\delta p} - i\omega\frac{\delta G_p}{\delta p}\right)\right|_{DC}\tilde{p} = 0 \end{cases} \tag{1.16}$$

The system 1.16 is solved considering the Dirichlet boundary condition $\tilde{n} = \tilde{p} = 0$ and assuming ohmic contacts.

1.2 Synopsys Sentaurus

This paragraph provides an overview of the software Synopsys Sentaurus. Fig.1.1 provides a reference for the description below regarding the connections between different parts of the software. The operating system on which the software is installed is linux CentOS. The outer layer is the tool Sentaurus Workbench (swb) that is capable of automatizing the operations necessary to study a problem and scheduling the run of the different tools in the suite.

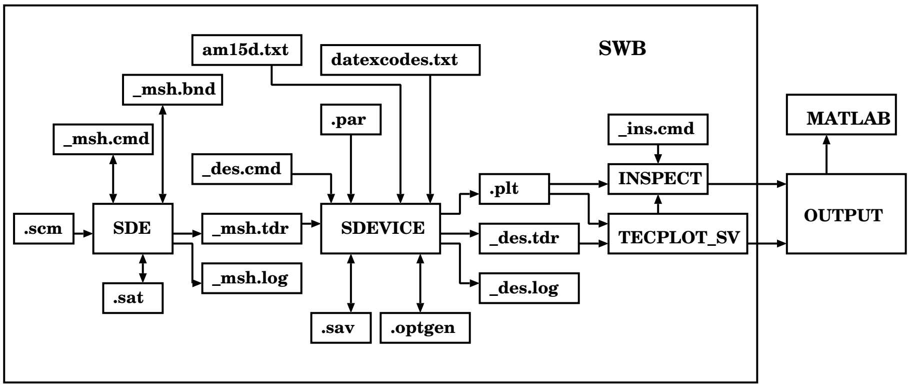
SWB
am15d.txt
datexcodes.txt
_msh.bnd
.par
_msh.cmd
_des.cmd
_ins.cmd
MATLAB
.plt
INSPECT
.scm
SDE
_msh.tdr
SDEVICE
_des.tdr
TECPLOT_SV
OUTPUT
.sat
_msh.log
_des.log
.sav
.optgen

Figure 1.1: Synopsys Sentaurus.

Starting from the left the first tool in the hierarchy is the Sentaurus Structure Editor (sde). With this tool physical structure, doping and materials are defined. The input can be given using a graphical user interface or defining a script (scm). The second method allows more flexibility and the definition of parameters for the Workbench. The *_msh.bnd*, *_msh.cmd*, *sat* and *_msh.log* files are created by Structure Editor for internal use while the *_msh.tdr* file is the file containing the definition of the structure to be used by the next tool.

The solution of the problem equations is discretised according to the structure defined in the *_msh.tdr* file and is calculated by Sentaurus Device (sdevice). The material parameters are defined in the *par* and *datexcodes.txt* files and the illumination spectrum is referred as *am15d.txt* in Fig. 1.1. Internal output files for Device are *sav*, *optgen* and *_des.log*; the *plt* file contains the electrical solution of the problem and the *_des.tdr* file gives a snapshot of the chosen physical quantities calculated for the structure defined in the *_msh.tdr* file for given working conditions (applied voltage, light intensity, temperature, frequency).

The tools Tecplot and Inspect are used to generate a graphical output of the solution and to exctract numerical data for further studies in other tools.

1.3 The discretization grid

The definition of the simulation grid requires a compromise between the accuracy of the solution and the calculation time. Especially for problems that see rapid variation of the physical quantities in more than one direction, e.g. the simulation of a polycristalline material, it is essential to control the distance between the mesh points using strict rules. Between the grid nodes the variation of stucture and material parameters is linearly interpolated [5, 6]. When solutions obtained for different structures (and therefore different simulation grids) are compared, we must consider the discretization error. In our grid definitions the precision has been evaluated to be higher than 1%.

Fig. 1.2 shows the meshing strategy of the *multibox* method in the Structure Editor. This method allows for very high accuracy close to interfaces and to relax it gradually as one moves away from the interface. The meshing points are placed by the tool according to *min step*, *max step* and *ratio*, defined separately for each direction. The min step is the initial distance between mesh points at the edge of the *multibox*, *max step* indicates the maximum distance between mesh points, and *ratio* is the relative variation of the distance alllowed when increasing the grid step. There can be multiple definitions for a region and the division will be made respecting all the definitions. Considering the division in one direction the distance d between the edges of a *multibox* will be covered according to eq. 1.17, where the division step is increased from the min to the max step.

$$d = \sum_{n=0}^{N} p_{min} r^{n} + \sum_{N+1}^{M} p_{max} \tag{1.17}$$

where p_{min} is the *min step*, p_{max} is the *max step*, r the *ratio*, M the total number of elements, N the number of division steps to reach the maximum.

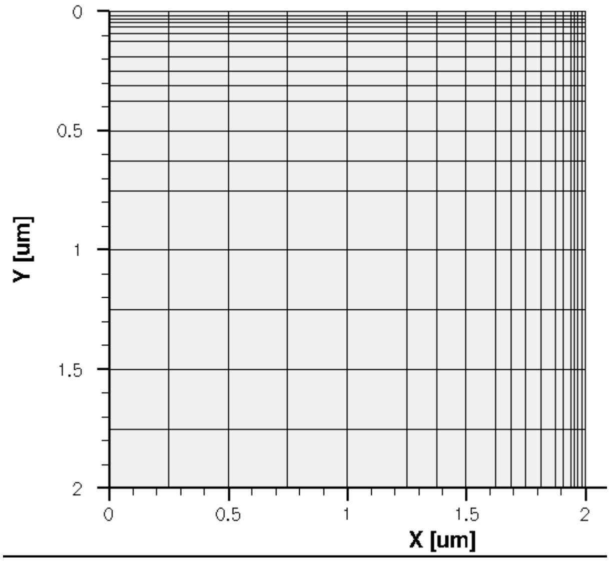

Figure 1.2: Multibox method used for meshing a square with 0.4 μm *min step*, 0.02 μm *max step*, and 1.5 *ratio* beetwen meshing points. The directions given to the meshing tool are -X and -Y.

1.4 Optics

The materials used in thin-film solar cells have a high optical absorption for photons with energy greater than the band gap. The optical behavior can be described in one dimension using a transfer matrix $T \in M^{2\times 2} : C^2 \to C^2$. This approach is exact when there is no scattering. This is true only for ideal interfaces and for layers with thickness smaller than the optical coherence length or bigger than the penetration depth. While interfaces can present high roughness and features with size comparable to the wavelengths of sunlight, hence the first hypothesis never holds, the second hypothesis is usually true. A different approach that can take scattering into account has been proposed by Charalambos [7]. Another non-ideal behavior comes from the polycrystalline nature of the materials. To fully explain the optics a bi- or tri- dimensional model would be necessary together with the knowledge of the local optical properties of the material; however, this information is difficult to obtain and no data is available about the optical properties of grain boundaries. The transfer matrix method is illustrated in Fig. 1.3, where Z_Σ and Z_Δ are defined according to equations 1.18 and 1.19.

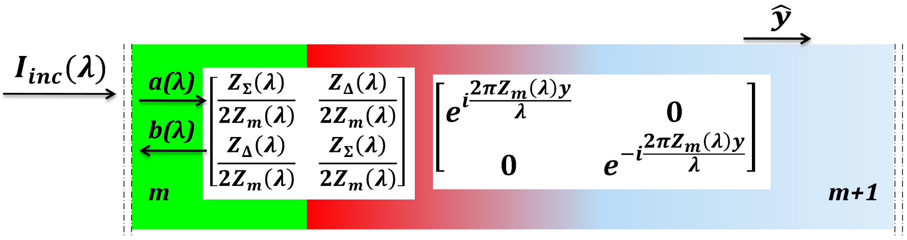
$\hat{y}$
$I_{inc}(\lambda)$
$a(\lambda)$
$b(\lambda)$
$\begin{bmatrix} \frac{Z_\Sigma(\lambda)}{2Z_m(\lambda)} & \frac{Z_\Delta(\lambda)}{2Z_m(\lambda)} \\ \frac{Z_\Delta(\lambda)}{2Z_m(\lambda)} & \frac{Z_\Sigma(\lambda)}{2Z_m(\lambda)} \end{bmatrix}$
$\begin{bmatrix} e^{i\frac{2\pi Z_m(\lambda)y}{\lambda}} & 0 \\ 0 & e^{-i\frac{2\pi Z_m(\lambda)y}{\lambda}} \end{bmatrix}$
m
m+1

Figure 1.3: Transfer matrix at a generic interface and inside a material for normal incident light.

$$Z_\Sigma(\lambda) = Z_m(\lambda) + Z_{m+1}(\lambda) \tag{1.18}$$

$$Z_\Delta(\lambda) = Z_m(\lambda) - Z_{m+1}(\lambda) \tag{1.19}$$

At every point of the structure the light is described by a forward propagating wave $a(\lambda)$ and a backward propagating wave $b(\lambda)$ related to the incident wave $I_{inc}(\lambda)$ by a product of matrices. In the considered case of normal incidence the complex wave impedance Z equals the complex refractive index $\tilde{n}$ of the media:

$$Z = \tilde{n} = n + ik \tag{1.20}$$

Where the real part n is the refractive index and the imaginary part k is the extinction coefficient and accounts for absorption. Multiplying the matrix at the interface (Fig. 1.3) by $[b(\lambda)\ a(\lambda)]^T$, the vector $[a(\lambda)\ b(\lambda)]^T$ is obtained for the waves at the left of the interface. In a similar way multiplying by $[a(\lambda)\ b(\lambda)]^T$ the matrix inside the material, the vector$[b(\lambda)\ a(\lambda)]^T$ is obtained for the waves at a distance y moving to the left from the considered point in Fig.1.3; in this tranformation there could be absorption of power if the indexes of the matrix are complex numbers (non-zero extinction coefficient). Considering coherent light, the ligth intensity $I(y,\lambda)$ at a considered point y and for a particular wavelength λ is given by eq. 1.21. In the last layer the backward propagating wave b is absent (the transmitted wave is absorbed by the surrounding media, e.g. the back contact of the cell) and the wave incident on the first layer is a known quantity. The resulting system of equations obtained from the product of all the transfer matrices of the studied structure has two equations and two unknowns. The complex waves at a given point of the structure can be related to the waves at one end of the structure allowing the calculation of intensity and generation for each point.

$$I(y,\lambda) = n(\lambda)\,|a(\lambda) + b(\lambda)|^2 I_{inc}(\lambda) \tag{1.21}$$

From the optical intensity I (eq. 1.21) the optical generation rate is calculated using eq. 1.22, where h is the Planck constant and c is the velocity of light in the vacuum.

$$G^{opt}(y,\lambda) = \frac{4\pi k(\lambda)\,I(y,\lambda)}{hc} \tag{1.22}$$

In the case of transparent media transmission and reflection are given by the well known Fresnel equations [8]. These are still valid for reflection if the incident media is lossless ($\tilde{n}_{incident} \in \mathscr{R}$), and for transmission if also the last material is lossless ($\tilde{n}_{last} \in \mathscr{R}$) and the reflected and transmitted waves have real vector of propagationl [8]. In the case of materials that absorb light ($\tilde{n} \in C$) the calculation through transfer matrices is needed. The absorption can be calculated by integrating the optical generation rate of eq. 1.22 according to eq. 1.23.

$$A = hc \int_{y_1}^{y_2} \int_{\lambda_1}^{\lambda_2} \frac{G^{opt}(y,\lambda)}{\lambda I_{inc}} dy d\lambda \tag{1.23}$$

Of particular meaning is the quantity obtained multiplying the integral of the optical generation rate by the electron charge q (eq. 1.24). It has the dimension of a current density and it is the current that would be extracted if every photon absorbed were converted into one eletron-hole pair (unity quantum yeld) and collected with unity quantum efficiency. This quantity gives extimation of the ideal maximum current for a given solar cell structure.

$$J_{OG} = q \int_{y_1}^{y_2} \int_{\lambda_1}^{\lambda_2} G^{opt}(y,\lambda)\, dy d\lambda \tag{1.24}$$

For example, considering a CIGS solar cell composed by the stacked structure $200nm$-ZnO/$50nm$-CdS/$3\mu m$-CIGS and the direct AM1.5 solar spectrum, the theoretical limit given by eq. 1.24 is $55mA/cm^2$, while this limit would be $75.5mA/cm^2$ assuming the total absorption of the solar spectrum.

The physical meaning of the transfer matrix method is conserved if we consider the Poynting vector, which represents the energy flux inside the material; energy conservation requires its continuity in the class C^0. Using the complex notation for the optical wave this vector assumes the form:

$$\vec{P}_m(y) = \frac{\Re\left\{z_m[a_{m,m+1}(y) + b_{m,m+1}(y)]^* \left[a_{m,m+1}(y) - b_{m,m+1}(y)\right]\right\}}{\Re\{z_0\}} \tag{1.25}$$

where z_0 is the impedance of the incident media and can be assumed unitary referring to the vacuum.

Chapter 2

Analytical models of the photocurrent

Numerical models allow to simulate arbitrary structures using complex model equation sets, while analytical models are generally based on simplified equations. However, the latter approach often provides a good compromise between model compactness and ease of integration into CAD tools on one side, and physical meaning and accuracy on the other. In this chapter an analytical model for the short-circuit current of a thin-film solar cell is developed with reference to a CIGS solar cell. The compact model is validated using numerical simulations of the structure ZnO/CdS/CIGS.

2.1 Thin-film solar cell structure

In a thin-film solar cell the basic idea is to absorb the sunlight in a layer with high optical absorption and good electrical properties. According to this idea, in the structure of Fig. 2.1 the first two layers are thinner and show high transmission, while the third layer is thick enough to absorb most of the photons with energy larger than the bandgap. If this last statement is true, the optical intensity in the absorber can be described by a single exponential term according to the Lambert-Beer law. Moreover, the optical coherence is likely to be longer than the thickness of the first two layers but smaller than the thickness of the absorber. For this reason and for the high optical density of the absorber (product of thickness and absorption coefficient), interference effects are significant only in the first two layers.

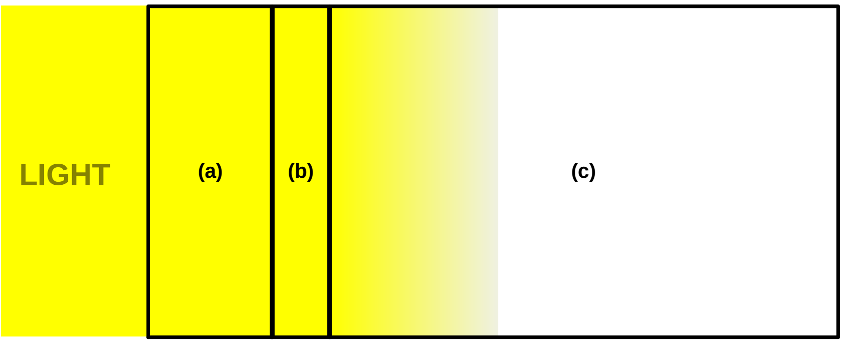

Figure 2.1: Basic structure of a CIGS solar cell: (a) window (ZnO), (b) buffer (CdS), (c) absorber (CIGS)

2.2 Contribution of the absorber

2.2.1 Quasi-neutral region

With reference to the coordinate system in Fig. 2.2, the diffusion equation for the minority carriers assumes the form [9, 10]:

$$\frac{d^2n}{dx^2} = \frac{n_p - n_{p0}}{L_n^2} - \frac{\alpha\Phi' e^{-\alpha x}}{D_n} \tag{2.1}$$

where $n_p - n_{p0}$ is the excess concentration of electrons with respect to equilibrium, L_n and D_n are the electron diffusion length and diffusion coefficient in the p-absorber; α is the absorption coefficient inside the absorber and Φ' is the photon flux entering the quasi-neutral region.

Using the depletion approximation, in short-circuit condition the junction law gives the first boundary condition:

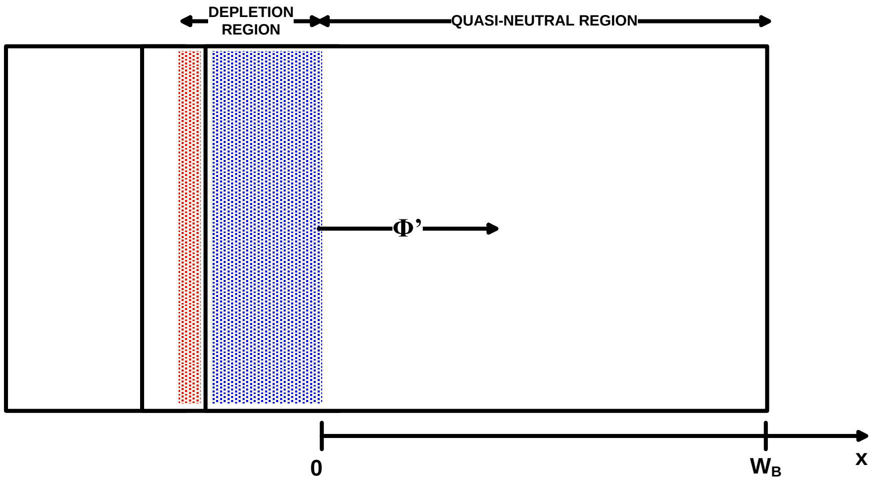

Figure 2.2: Coordinate system for the quasi-neutral region of the absorber.

$$n_p(0) - n_{p0} = 0 \tag{2.2}$$

The second condition is different depending on the thickness W_B of the quasi-neutral region and the electron diffusion length L_n. When W_B is greater than L_n, (long base, LB), the second boundary condition is eq. 2.3. When W_B is lower than L_n (short base, SB), the second boundary condition is eq. 2.4, obtained considering ohmic contact at $x = W_B$.

$$\lim_{x \to +\infty} n_p(x) - n_{p0} = 0 \tag{2.3}$$

$$n_p(W_B) - n_{p0} = 0 \tag{2.4}$$

Therefore we have two different Cauchy problems given by eqs. 2.1, 2.2 and 2.3 and by eqs. 2.1, 2.2 and 2.4. Their solutions are, respectively:

$$n_p^{LB}(x) = n_{p0} + \frac{\alpha\,\Phi' \mathrm{L}_n^2}{D_n\,(\alpha^2 \mathrm{L}_n^2 - 1)} \left[\mathrm{e}^{-\frac{x}{L_n}} - \mathrm{e}^{-\alpha x} \right] \tag{2.5}$$

$$n_p^{SB}(x) = n_{p0} + \frac{\alpha\,\Phi' \mathrm{L}_n^2}{D_n\,(\alpha^2 \mathrm{L}_n^2 - 1)} \left[\frac{sinh\left(\frac{x}{L_n}\right) e^{-\alpha W_B} - sinh\left(\frac{x}{L_n} - \frac{W_B}{L_n}\right)}{sinh\left(\frac{W_B}{L_n}\right)} - e^{-\alpha x} \right] \tag{2.6}$$

For the neutrality of charge in the quasi-neutral region, the electron current due to the excess of carriers in the absorber is:

$$J_{SC} = qD_n \left.\frac{dn}{dx}\right|_{x=0} . \tag{2.7}$$

Using eqs. 2.5 and 2.6 in eq. 2.7, for the long base and the short base cases, the current contribution of the quasi-neutral region is given by eqs. 2.8 and 2.9, respectively:

$$J_{SC,n}{}^{LB} = q\Phi' \frac{\alpha L_n}{(\alpha L_n + 1)} \tag{2.8}$$

$$J_{SC,n}{}^{SB} = q\Phi' \frac{\alpha L_n}{(\alpha^2 L_n^2 - 1)} \left[\alpha L_n + \frac{\left(\mathrm{e}^{-\alpha W_B} - \cosh\left(\frac{\mathrm{W}_B}{\mathrm{L}_n}\right)\right)}{\sinh\left(\frac{\mathrm{W}_B}{\mathrm{L}_n}\right)} \right] \tag{2.9}$$

Eq. 2.9 has a singularity at $\alpha L_n = 1$ that assumes the finite value of:

$$\lim_{\alpha \to \frac{1}{L_n}} J_{SC,n}{}^{SB} = q\Phi' \left(\frac{1}{2} - \frac{\alpha \mathrm{W}_B}{\mathrm{e}^{2\alpha \mathrm{W}_B} - 1} \right) = q\Phi' \left(\frac{1}{2} - \frac{\mathrm{W}_B}{\mathrm{L}_n \left(\mathrm{e}^{2\frac{\mathrm{W}_B}{L_n}} - 1 \right)} \right) \tag{2.10}$$

The limit for W_B that goes to infinity of eq. 2.9 is coincident with the long base case of eq. 2.8:

$$\lim_{W_B \to +\infty} {J_{SC,n}}^{SB} = {J_{SC,n}}^{LB} = q\Phi' \frac{\alpha L_n}{(\alpha L_n + 1)} \tag{2.11}$$

Long base and short base equations are also very close to each other for $W_B > L_n$ and they can be approximated as in the limit case of eq. 2.11. Based upon this consideration the short base equation 2.9 can be assumed valid even if the quasi-neutral absorber region is thicker than the electron diffusion length.

Eq. 2.9, normalized to its maximum value $q\Phi'$, gives the portion of the current generated in the absorber quasi-neutral region reaching the contacts. This normalized photocurrent is plotted in Fig. 2.3 as a function of the diffusion length L_n and the depletion region width W_B, for three different values of the absorption coefficient α.

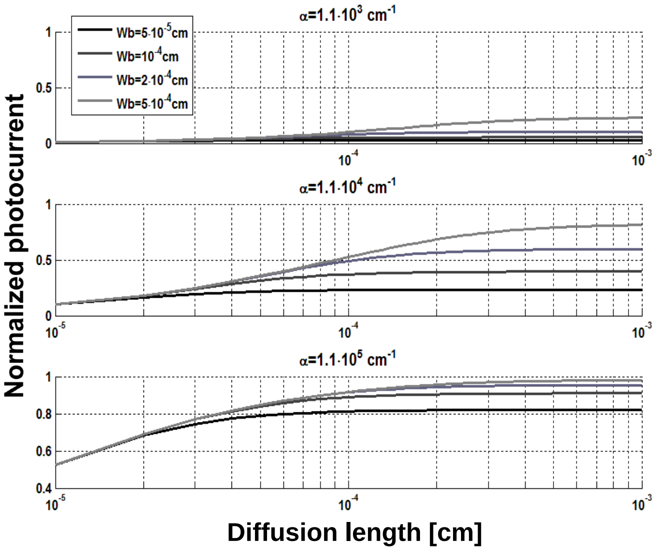

Figure 2.3: Collection of the current generated optically in the quasi-neutral region of the absorber (eq. 2.9) and normalized to its maximum value $q\Phi'$ at the interface with the previous layer.

2.2.2 Depletion region

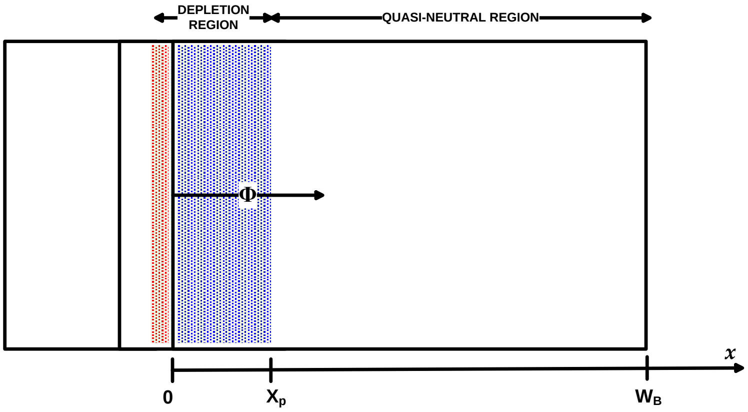

Figure 2.4: Coordinate system for the depletion region of the absorber.

Under short-circuit condition the junction law sets to zero the excess carrier concentration at the edge of the depletion region. Assuming the quasi-Fermi levels to be constant inside the depletion region, the excess carrier concentration is null also inside the depletion region and therefore there is no Shockley-Read-Hall recombination:

$$R = \frac{N_t v_{th}^n v_{th}^p \sigma_n \sigma_p (np - n_i^2)}{v_{th}^n \sigma_n (n + n_i e^{\frac{E_t - E_i}{kT}}) + v_{th}^p \sigma_p (p + n_i e^{\frac{E_i - E_t}{kT}})} = 0 \qquad (2.12)$$

This last assumption is an approximation that results reasonable for thin film solar cells (under short-circuit condition), e.g. in the CIGS case numerical simulations show that the recombination term is at least two order of magnitude smaller than the generation term inside the depletion region under short-circuit condition.
Assuming eq. 2.12 valid, the current due to generation in the space charge region of the absorber is:

$$J_D^{absorber} = q\int_0^{X_p} \alpha\Phi e^{-\alpha x}dx = q\Phi\left[1 - e^{-\alpha X_p}\right] \tag{2.13}$$

where the depletion region width in eq. 2.13 can be calculated using eq. 2.14, according to the classical hetero-junction theory [11]:

$$X_p = \sqrt{\frac{2\kappa_p\kappa_n\varepsilon_0 N_D V_{bi}}{qN_A(N_a\kappa_p + N_D\kappa_n)}} \tag{2.14}$$

with

$$V_{bi} = \frac{kT}{q}\log\left(\frac{N_A N_D}{n_{i,n}n_{i,p}}\right) + (\chi_p - \chi_n) + \frac{E_{G,p} - E_{G,n}}{2} - \frac{kT}{2q}\log\left(\frac{N_{V,p}N_{C,n}}{N_{C,p}N_{V,n}}\right) \tag{2.15}$$

where κ_n, κ_p are the relative dielectric constants of buffer and absorber (layers (b) and (c) in Fig. 2.1); $n_{i,n}$, $n_{i,p}$ the intrinsic concentrations; χ_n, χ_p the electron affinities; $E_{g,n}$, $E_{g,p}$ the band gaps; $N_{V,n}$ $N_{V,p}$ the effective densities of states in the valence bands; $N_{C,n}$, $N_{C,p}$ the effective densities of states in the conduction bands; N_D, N_A donor and acceptor doping.

2.3 Photon flux calculation

As shown in Fig. 2.5, the structure is made of the three layers, characterized by complex refractive index and thickness. Together with the angle of incidence, this information allows to compute the wave impedance for TE and TM modes. In particular, for normal incidence the wave impedance is the complex refractive index. For non-normal incidence the wave impedance is increased or decreased depending on the polarization and the angle of incidence; however, the following calculation is still valid. We denote the wave impedances of the materials in Fig. 2.5 with z1, z2 and z3, and the incident and reflected waves at the interfaces between materials with a and b respectively, with suffixes as defined in Fig. 2.5.

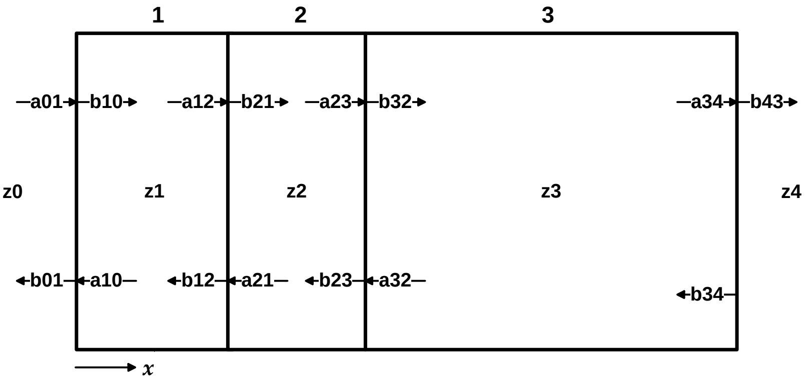

Figure 2.5: Optical waves in a three-layer structure.

The relation between waves at an interface between two materials m and $m+1$, for normal incidence, is [7, 12]:

$$\begin{bmatrix} b_{m,m+1} \\ \\ a_{m,m+1} \end{bmatrix} = \begin{bmatrix} \frac{z_m+z_{m+1}}{2z_m} & \frac{z_m-z_{m+1}}{2z_m} \\ \frac{z_m-z_{m+1}}{2z_m} & \frac{z_m+z_{m+1}}{2z_m} \end{bmatrix} \begin{bmatrix} a_{m+1,m} \\ \\ b_{m+1,m} \end{bmatrix} = \left[TM^{m,m+1}\right] \begin{bmatrix} a_{m+1,m} \\ \\ b_{m+1,m} \end{bmatrix} \tag{2.16}$$

with $z_m = n_m + ik_m$, where n_m and k_m are refraction and extinction coefficients for the material m.

The propagation in direction x inside a media m, for normal incidence, is:

$$\begin{bmatrix} a_{m,m-1}(x) \\ \\ b_{m,m-1}(x) \end{bmatrix} = \begin{bmatrix} e^{i\frac{2\pi z_m x}{\lambda}} & 0 \\ 0 & e^{-i\frac{2\pi z_m x}{\lambda}} \end{bmatrix} \begin{bmatrix} b_{m,m+1} \\ \\ a_{m,m+1} \end{bmatrix} = \left[TM^{m,m}\right] \begin{bmatrix} b_{m,m+1} \\ \\ a_{m,m+1} \end{bmatrix} \tag{2.17}$$

where λ is the wavelength of incident light. Combining eqs. 2.16 and 2.17 we can calculate the relation between $[a\,b]^T$ at a generic position x and another point in the structure:

$$\begin{bmatrix} a_{m,m-1}(x) \\ \\ b_{m,m-1}(x) \end{bmatrix} = \left[TM^{m,m}(x)\right]\left[TM^{m,m+1}\right]\prod_{q=m+1}^{Q}\left[TM^{q,q}(d_q)\right]\left[TM^{q,q+1}\right]\begin{bmatrix} a_{Q+1,Q} \\ \\ b_{Q+1,Q} \end{bmatrix} \tag{2.18}$$

where d_q is the thickness of layer q. Considering the whole structure the term $a_{0,1}$ is the incident power and the boundary condition of the last layer is $a_{Q+1,Q} = 0$. With these considerations eq. 2.18 with $x = d_1$ and multiplied by TM^{01} on the right provides two equations with two unknowns $b_{0,1}$ and $b_{Q+1,Q}$: they are the reflected and transmitted waves. In the three-layer structure the third layer is the absorber of the solar cell and its optical behavior can be described neglecting b34 for the wavelength of interest. This is justified by a thickness d_3 big enough to prevent the light from reaching the back contact. Under this assumption the photon flux of wave b32 can be described by a single exponential term and eqs. 2.9 and 2.13 are valid.

We calculate now the photon flux due to wave b32.
With the previous considerations on eq. 2.18, the normalized complex transmission coefficient is:

$$t = \frac{t_{01}t_{12}t_{23}}{e^{\frac{2\pi i}{\lambda}d_2}\left(e^{\frac{2\pi i}{\lambda}d_1} + \mathrm{r}_{01}\mathrm{r}_{12}\,e^{-\frac{2\pi i}{\lambda}d_1}\right) + \mathrm{r}_{23}\,e^{-\frac{2\pi i}{\lambda}d_2}\left(\mathrm{r}_{01}\,e^{-\frac{2\pi i}{\lambda}d_1} + \mathrm{r}_{12}\,e^{\frac{2\pi i}{\lambda}d_1}\right)} \tag{2.19}$$

where

$$t_{m,m+1} = \frac{2\,\mathrm{z}_m}{\mathrm{z}_m + \mathrm{z}_{m+1}}; \quad r_{m,m+1} = \frac{\mathrm{z}_m - \mathrm{z}_{m+1}}{\mathrm{z}_m + \mathrm{z}_{m+1}}$$

The transmission coefficient is:

$$T = \Re\left\{\frac{z_3}{z_0}\right\}\|t\|^2 \tag{2.20}$$

From eq. 2.20, and being I_{inc} the intensity of the light incident on layer 1 from the left at wavelength λ, the photon flux inside layer 3 is:

$$\Phi(x) = T\frac{\lambda I_{inc}}{hc}e^{\frac{-4\pi\Im\{z_3\}x}{\lambda}} = T\Phi_{inc}e^{-\alpha x} \tag{2.21}$$

where the x axis has its origin as shown in Fig. 2.5.

2.4 Numerical validation

The model is validated by the Synopsys Sentaurus numerical simulation of a structure with the parameters reported in Tab. 2.1 and Tab. 2.2. The concentration of traps and doping in the CIGS absorber are varied to test the model under different conditions.

Property	ZnO	CdS	CIGS
Type	acceptor	acceptor	acceptor
Density $[cm^{-3}]$	10^{16}	$5 \cdot 10^{16}$	N_b
Position	midgap	midgap	midgap
σ_e $[cm^2]$	10^{-16}	10^{-15}	$2 \cdot 10^{-14}$
σ_p $[cm^2]$	10^{-13}	10^{-12}	$2 \cdot 10^{-14}$

Table 2.1: Trap parameters for the validation of the analytical model of the photocurrent.

We consider now the approximation b34=0. Fig. 2.6 shows the optical intensity with and without the contribute of b34. This provides a qualitative idea of the approximation we are making; a more quantitative evaluation of the approximation is in Fig.2.7, where the optical generation rate (closely related with the current) is calculated with and without b34. We do not compare the photon flux since, according to equation 2.1, its weight on the current is not constant and depends on absorption. From the good agreement in Fig. 2.7, we can conclude that the approximation is rea-

Property	ZnO	CdS	CIGS
E$_{GAP}$ [eV]	3.3	2.4	1.15
χ [eV]	4.6	4.6	4.6
Doping type	n	n	p
$\|N_D - N_A\| \quad [cm^{-3}]$	10^{18}	$5 \cdot 10^{17}$	N_A
$\frac{\varepsilon}{\varepsilon_0}$	9	10	13.6
$\frac{m_e}{m_0}$	0.2	0.2	0.09
$\frac{m_h}{m_0}$	1.2	0.8	0.72
$\mu_e \quad \left[\frac{cm^2}{Vs}\right]$	100	100	100
$\mu_h \quad \left[\frac{cm^2}{Vs}\right]$	25	25	12.5

Table 2.2: Material parameters for the validation of the photocurrent analytical model.

sonable. This also demonstrates that the optical coherence length in the absorber of a thin-film solar cell has low influence on the optical generation.

Eqs. 2.22 and 2.23 give the optical intensity and generation for a generic material m.

$$I_m(x) = \Re\{z_m\} \|a_{m,m+1}(x) + b_{m,m+1}(x)\|^2 I_{inc} \tag{2.22}$$

$$G_m(x) = \frac{4\pi \Im\{z_m\} I_m(x)}{hc} \tag{2.23}$$

Since the main current contribution comes from generation in the absorber, we first approximate the generation in the first two layers using a current offset and look at the result given by eqs. 2.9 and 2.13. The comparison between the compact model and the numerical simulation is in Fig. 2.8. The maximum relative difference between

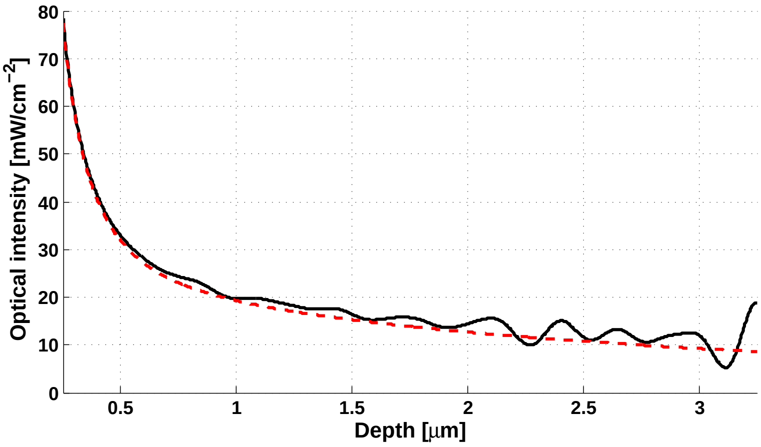

Figure 2.6: Continuous line: optical intensity calculated considering the interference of all layers. Dashed line: optical intensity calculated neglecting the reflected wave b34 in the absorber.

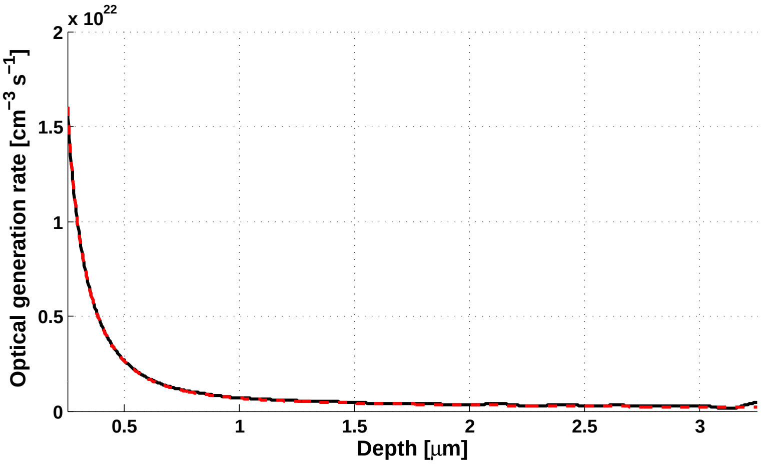

Figure 2.7: Continuous line: optical generation rate calculated considering the interference of all layers. Dashed line: optical generation rate calculated neglecting the reflected wave b34 in the absorber.

the two models is 2.8 %. This difference is due partly to the discretization error of the numerical simulation and partly to the approximations of the compact model.

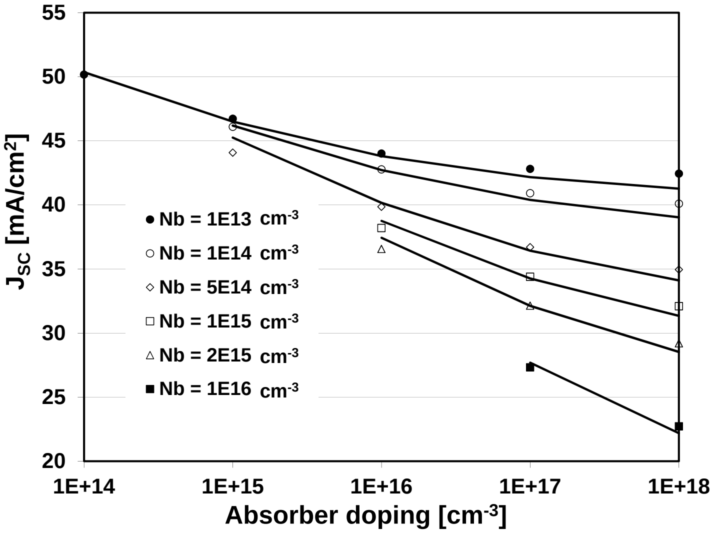

Figure 2.8: Short circuit current calculated considering the absorber space charge and quasi-neutral terms and adding a constant value of $2.2 mA/cm^2$ to take into account the first two layers. The result is obtained for different concentrations of deep states N_b in the absorber as a function of doping. The symbols denote the numerical simulations and the solid lines the compact model developed.

2.5 Contribution of the first layers

The first two layers of Fig. 2.9 represent general window and buffer layers. We assume their thickness is small compared to the optical coherence length: this allows to calculate the interference using the transfer matrix method. Considering also the thickness of the two layers smaller than the useful wavelengths (solar spectrum above the band gap), the optical intensity and generation rate can be considered to be approximately constant rather than expontial with the position. We assume therefore a

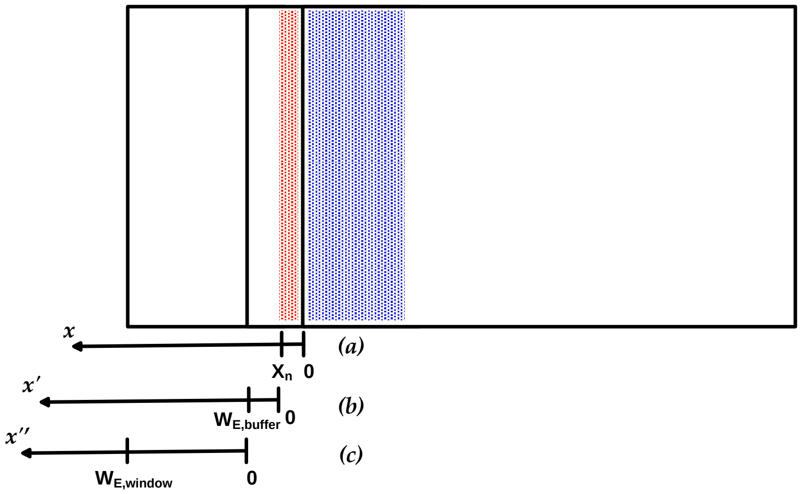

Figure 2.9: Coordinate system for window and buffer layers. (a) Buffer depletion region; (b) buffer quasi-neutral region; (c) window quasi-neutral region.

constant generation term to calculate the current. With reference to case (b) and case (c) of Fig. 2.9, the Cauchy problem to solve is 2.24 for the quasi-neutral region of the window layer, and 2.25 for the quasi-neutral region of the buffer layer.

$$\begin{cases} \frac{d^2p}{dx^2} = \frac{p_n - p_{n0}}{L_p^2} - \frac{G_L}{D_p} \\ p_n(0) - p_{n0} = 0 \\ p_n(W_{E,a}) - p_{n0} = 0 \end{cases} \tag{2.24}$$

$$\begin{cases} \frac{d^2p}{dx^2} = \frac{p_n - p_{n0}}{L_p^2} - \frac{G_L}{D_p} \\ p_n(0) - p_{n0} = 0 \\ p_n(W_{E,b}) - p_{n0} = 0 \end{cases} \tag{2.25}$$

Eqs. 2.24 and 2.25 are obtained with the following boundary conditions: *(i)* short base: this is most likely always true for the typical thickness of these layers (Tab. 2.2); *(ii)* ohmic contact: this is valid for the window layer and also for the buffer layer

since the window layer acts as ohmic contact for holes in this case: in fact, the valence band discontinuity reduces the hole concentration in proximity of the heterojunction as if there was an ohmic contact at $x = W_{E,buffer}$ in Fig. 2.9.
The solution of the Cauchy problems in eqs. 2.24 and 2.25 is eq. 2.26, where the x-axis is defined in Fig. 2.9.

$$p_n(x) = p_{n0} + \tau_p G_L \left(1 - \frac{\sinh\left(\frac{\mathrm{W}_B - x}{\mathrm{L}_p}\right) + \sinh\left(\frac{x}{\mathrm{L}_p}\right)}{\sinh\left(\frac{\mathrm{W}_B}{\mathrm{L}_p}\right)} \right) \tag{2.26}$$

From the charge neutrality in the quasi-neutral regions, the electron current due to the excess of carriers is the solution of eq. 2.27. From eqs. 2.26 and 2.27, the expressions of current the due to the quasi-neutral region of the first two layers is given by eqs.2.28.

$$J_{SC} = qD_p \left. \frac{dp}{dx} \right|_{x=0} \tag{2.27}$$

$$\begin{aligned} J_{SC,p}^{buffer} &= qG_L \tanh\left(\frac{W_{E,buffer}}{2L_p}\right) \\ J_{SC,p}^{window} &= qG_L \tanh\left(\frac{W_{E,window}}{2L_p}\right) \end{aligned} \tag{2.28}$$

If the diffusion length is large compared to the layer thickness, we can use the limit in eq. 2.29 to calculate the current [13].

$$\lim_{L_p \to \infty} J_{SC,p} = \frac{qG_L W_E}{2} \tag{2.29}$$

For the generation in the depletion region of the buffer layer, considering a constant generation term G_L, we obtain the result of eq. 2.30.

$$J_D^{buffer} = q \int_0^{X_n} G_L dx = qG_L X_n \tag{2.30}$$

The extension of the depletion width in eq. 2.30 is calculated using eq. 2.31, assuming the doping is high enough for the buffer to be not fully depleted.

$$X_n = \sqrt{\frac{2\kappa_p \kappa_{n0} N_A V_{bi}}{q N_D (N_D \kappa_n + N_A \kappa_p)}} \tag{2.31}$$

The mean value of generation is obtained from the complex waves calculated using eq. 2.18 written for the considered layer and integrated over space, according to eq. 2.32.

$$\overline{G_{Lm}(x)} = \frac{1}{d_m} \int_0^{d_m} 4\pi \Im\{z_m\} \Re\{z_m\} \left\| a_{m,m+1}(x) + b_{m,m+1}(x) \right\|^2 dx \tag{2.32}$$

Eq. 2.32 becomes eq. 2.33 for the buffer layer and eq. 2.34 for the window layer.

$$\overline{G_{L2}(x)} = \frac{1}{d_2} \int_0^{d_2} \frac{4\,\pi\,\mathrm{k}_2\,\mathrm{n}_2 \left| \mathrm{r}_{23}\,\mathrm{e}^{\mathrm{i}(\mathrm{d}_1\,\varphi_1 + \mathrm{d}_2\,\varphi_2)} + \mathrm{e}^{\mathrm{i}[\mathrm{d}_1\,\varphi_1 + (\mathrm{d}_2 + 2x)\,\varphi_2]} \right|^2 |\mathrm{t}_{01}|^2\,|\mathrm{t}_{12}|^2}{\left| \mathrm{e}^{\mathrm{i}[2\mathrm{d}_1\,\varphi_1 + (2\mathrm{d}_2 + x)\,\varphi_2]} + \mathrm{r}_{01}\,\mathrm{r}_{12}\mathrm{e}^{\mathrm{i}\varphi_2(2\mathrm{d}_2 + x)} + \mathrm{r}_{12}\,\mathrm{r}_{23}\,\mathrm{e}^{\mathrm{i}(2\mathrm{d}_1\,\varphi_1 + x\varphi_2)} + \mathrm{r}_{01}\,\mathrm{r}_{23}\,\mathrm{e}^{\mathrm{i}\varphi_2 x} \right|^2} dx \tag{2.33}$$

$$\overline{G_{L1}(x)} = \frac{1}{d_1} \int_0^{d_1} \frac{4\pi \mathrm{k}_1 \mathrm{n}_1 \left| \mathrm{r}_{23}\, \mathrm{e}^{\mathrm{i}\mathrm{d}_1 \varphi_1} + \mathrm{r}_{12} \mathrm{e}^{\mathrm{i}(\mathrm{d}_1 \varphi_1 + 2\mathrm{d}_2 \varphi_2)} + \mathrm{e}^{\mathrm{i}[\mathrm{d}_1 \varphi_1 + 2(\mathrm{d}_2 \varphi_2 + \varphi_1 x)]} + \mathrm{r}_{12}\, \mathrm{r}_{23}\, \mathrm{e}^{\mathrm{i}(\mathrm{d}_1 \varphi_1 + 2\varphi_1 x)} \right|^2 |\mathrm{t}_{01}|^2}{\left| \mathrm{e}^{\mathrm{i}[2\mathrm{d}_1 \varphi_1 + 2\mathrm{d}_2 \varphi_2 + \varphi_1 x]} + \mathrm{r}_{01}\, \mathrm{r}_{12} \mathrm{e}^{\mathrm{i}(2\mathrm{d}_2 \varphi_2 + \varphi_1 x)} + \mathrm{r}_{12}\, \mathrm{r}_{23}\, \mathrm{e}^{\mathrm{i}\varphi_1 (2\mathrm{d}_1 + x)} + \mathrm{r}_{01}\, \mathrm{r}_{23}\, \mathrm{e}^{\mathrm{i}\varphi_1 x} \right|^2} dx \tag{2.34}$$

where:

$$\varphi_m = \frac{2\pi z_m}{\lambda} \tag{2.35}$$

The results of eqs. 2.33 and 2.34, multiplied by the thickness of the layer and the electron charge, provide the maximum current contribution of the first two layers. In the considered case, it is $3.71 mA/cm^2$ for the ZnO layer and $1.76 mA/cm^2$ for the CdS layer.

Considering all the contributions, the maximum relative difference between the analytical model and the numerical simulation is 2.1 %, due to spatial discretization and approximations of the compact model. Fig. 2.10 shows the result of the complete calculation: there is an improvement with respect the case of Fig. 2.8. In particular, we can see that the effect of the absorber doping on the depletion region width x_n in the buffer layer is now modeled better for the lower absorber doping.

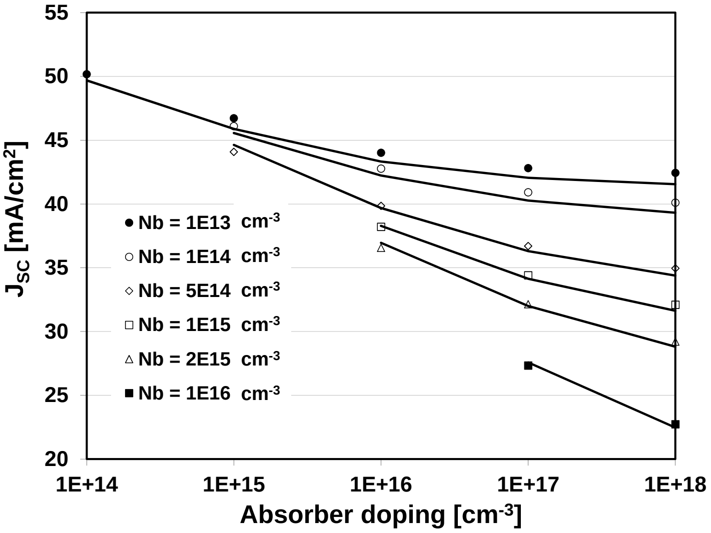

Figure 2.10: Short-circuit current calculated considering all terms. The result is obtained for different concentrations of deep states N_b in the absorber as a function of doping. The symbols denote the numerical simulations and the solid lines the compact model.

2.6 Summary

The good agreement between the numerical simulations and the analytical model shows the validity of the approximations over a large range of doping and deep state concentrations. Buffer and windows layers have a small impact on the short-circuit current, and constant optical generation can be assumed. The current in the absorber is obtained considering exponential generation and its contribute is increased with decreasing doping. From the transport analysis in the quasi-neutral region we see how increasing the diffusion length (lower trap density) the short circuit current can also be increased. A longer diffusion length allows higher doping in the absorber without a drastical decrease of the current, which is an advantage to obtain high open circuit voltage.

Chapter 3

Polycrystalline CIGS

Thin-film solar cells based on Cu(In,Ga)Se_2 (CIGS) show record efficiencies among thin-film technologies, and are now experiencing the first phase of commercialization, with manufacturers introducing mass production processes yielding cells with efficiencies in the 13-15% range [1]. Lab specimens can provide power conversion efficiency as high as 20% [2], despite the poly-crystalline structure of the semiconductor thin film. The structure of the most popular cells features, from top to bottom, a ZnO transparent contact layer, an n-doped CdS buffer layer, a p-doped CIGS absorber layer, and a backside metal (Mo) contact sitting on a soda lime glass or flexible substrate. Several papers were published on material growth, processing and characterization on one side, and on the performance of finished cells and modules on the other, but there is still a gap to fill in between: some of the specific features of CIGS cells, specifically those pertaining to the behavior of grain boundaries and heterojunctions, are still under debate, and a complete understanding of the relationship between material characteristics and cell behavior is not available yet. Since data about defects, band offsets, potential spikes, etc., at grain boundaries and interfaces are hard to obtain experimentally, and often indirect and speculative, some researchers have tried to bridge the gap using physical-level numerical simulations [14, 15, 16, 17]. In this chapter numerical simulations are used to investigate the specific features of these devices, with the ultimate goal of developing physics-based compact models for quick assessment of the performance of cells and modules under development at CNR-IMEM, Parma, Italy.

3.1 CIGS solar cell numerical modeling

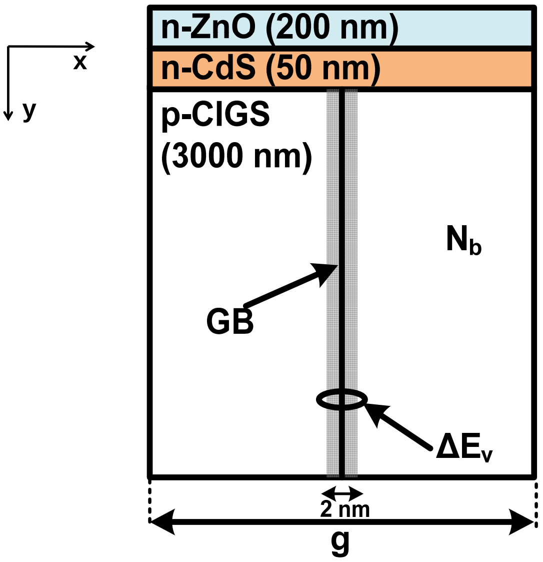

Figure 3.1: Structure of the simulated solar cell. g is the grain size. The region around the GB represents Cu-poor CIGS.

The behavior of defects at grain boundaries (GBs), in the grain interior (GI), and at hetero-interfaces is critical for the performance of CIGS solar cells. In particular it is known that: (i) the p-doped CIGS absorber has a columnar polycrystalline structure, with grains in the micrometer range; (ii) this polycrystalline structure does not have a disruptive effect on cell performance, probably due to charged defects and/or band offsets preventing the GBs from acting as effective recombination centers [18]; (iii) Cu-poor regions are likely to form at GBs and at the top CIGS interface, resulting in localized wider band-gap and valence band offset [19]. We focus on standard n-ZnO/n-CdS/p-Cu(In$_{0.69}$Ga$_{0.31}$)Se$_2$ cells (Fig. 3.1). Symmetry and periodicity allow to limit the simulated area to one grain boundary, provided that the grain size is reasonably uniform over the cell area. All the simulations are performed using Synopsys Sentaurus. The cell behavior in the dark is described by the Poisson, electron and hole continuity and drift-diffusion equations. Recombination via deep defects follows the Shockley-Read-Hall (SRH) model. Deep traps are located in the GI (bulk acceptors) [14], and at the GB (interface donors) [15], the Cu-poor region at the GB may feature an increased band-gap totally localized on the valance band, ΔEV (i.e., ΔEC = 0) [19]. Fig. 3.2 shows the energy band profile along a horizontal line in the vicinity of a GB (with ΔEV = 0.2 eV). The surface donors at the GB result in a downward bend of the energy bands that enhances the GB of electrons and depletes it of holes; in the presence of a valence band offset due to Cu depletion, the hole concentration is further reduced, which is beneficial to the cell in that it reduces non-radiative recombination at the GB.

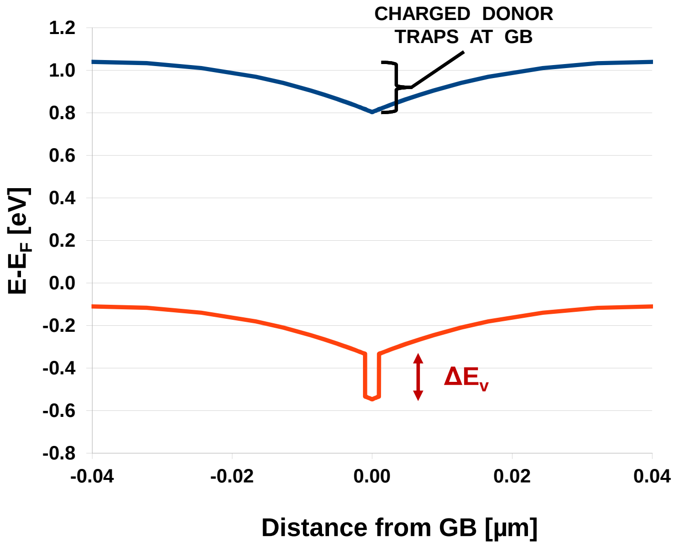

Figure 3.2: Energy band profile along a horizontal line in the CIGS (see Fig. 3.1). The grain boundary hosts interface donors and is characterized by a valence band offset ΔEV (0.2 eV in this example).

The full set of material parameters used in the simulations of the baseline cell is shown in Tab. 3.1. The cell is illuminated by the standard AM1.5D solar spectrum.

Layer	**ZnO**	**CdS**	**CIGS**
E_G [eV]	3.3	2.4	1.15
χ [eV]	4.6	4.6	4.6
Doping $[cm^{-3}]$	$N_D = 10^{18}$	$N_D = 6 \cdot 10^{17}$	$N_A = 3 \cdot 10^{17}$
$\frac{\varepsilon}{\varepsilon_0}$	9	10	13.6
$\frac{m_e}{m_0}$	0.2	0.2	0.09
$\frac{m_h}{m_0}$	1.2	0.8	0.72
$\mu_e \quad \left[\frac{cm^2}{Vs}\right]$	100	100	100
$\mu_h \quad \left[\frac{cm^2}{Vs}\right]$	25	25	12.5
Bulk traps	**ZnO**	**CdS**	**CIGS**
Energy [eV]	midgap	midgap	midgap
$\sigma_e \quad [cm^2]$	10^{-16}	10^{-15}	$2 \cdot 10^{-14}$
$\sigma_h \quad [cm^2]$	10^{-13}	10^{-12}	$2 \cdot 10^{-14}$
Density $\quad [cm^{-3}]$	10^{16}	10^{16}	$2 \cdot 10^{15}$
GB traps	**Density**	**Energy [eV]**	$\sigma_e = \sigma_h$
Donor	$2 \cdot 10^{12} cm^{-2}$	$E_V + 0.88$	$10^{-15} cm^2$

Table 3.1: Polycrystalline CIGS material parameters.

Fig. 3.3 shows the effect of the grain size g on the efficiency η (defined as the ratio between the output power at the maximum power point and the incident radiation power), for three different values of the valence band discontinuity at the GB, ΔEV. As previously observed, the valence band offset at the GB hinders hole collection by the GB (see Fig. 3.2), thus reducing the recombination at GB defects; with $\Delta E_V = 0.4$ eV the GB is practically passivated. As expected, as the grain size increases, η tends to the single-crystal value > 17%. It is interesting to notice that a grain size variation in the 0.5-2 μm range, quite plausible for current manufacturing processes, results in a significant difference in η unless the GB is passivated by a large ΔE_V.

A similar behavior as a function of grain size and valence band discontinuity appears on the open circuit voltage (Fig. 3.4), short circuit current (Fig. 3.5) and fill factor (Fig. 3.6). However, the passivation for the intermediate value of valence band discontinuity, $\Delta E_V = 0.2$ eV, is higher for the open circuit voltage and the fill factor. In fact, the valence band discontinuity is very effective in reducing the hole concentration at GBs, preventing them from acting as a shunting path; while from the point of view of the short-circuit current the passitivation requires a further reduction of hole concentration at GBs (ΔEV = 0.4 eV) to make holes the limiting factor for recombination.

In the following a compact model of the cell's behavior in the dark is developed, with reference to the smallest grain size considered (g=0.5 μm) to model the polycrystalline behavior.

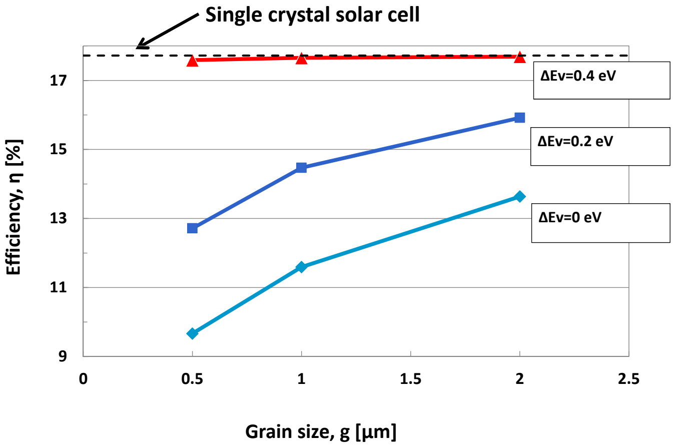

Figure 3.3: Effect of CIGS grain size on the efficiency, for different values of the GB valence-band discontinuity.

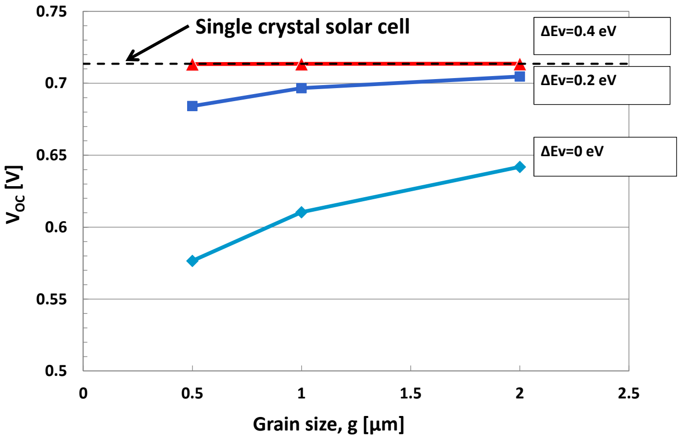

Figure 3.4: Effect of CIGS grain size on the open circuit voltage, for different values of the GB valence-band discontinuity

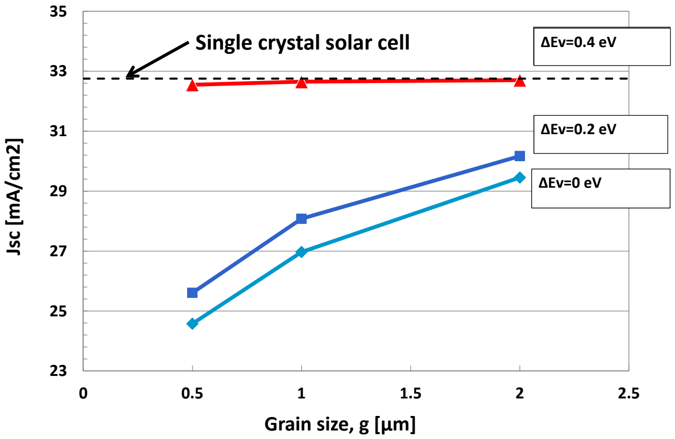

Figure 3.5: Effect of CIGS grain size on the short circuit current, for different values of the GB valence-band discontinuity

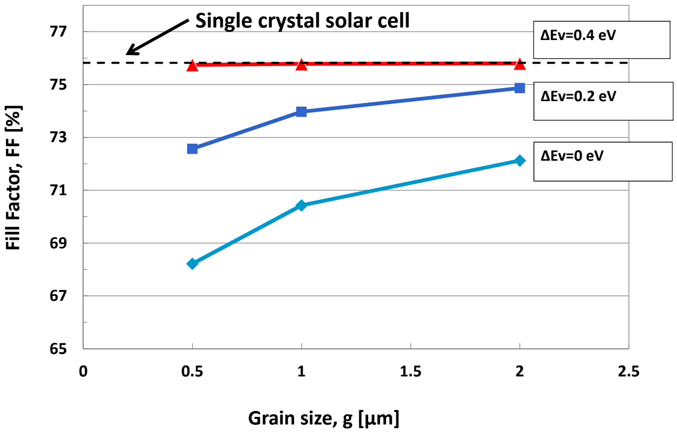

Figure 3.6: Effect of CIGS grain size on the fill factor, for different values of the GB valence-band discontinuity.

3.2 Compact modeling of the dark i-v curve

In the absence of defect-rich grain boundaries, i.e. in the case of a syngle-crystal cell, the dark I-V curve can be satisfactorily described by a standard two-diode model, where a diode with ideality factor $n_I = 1$ describes the ideal diode current component, and a diode with $n_{SC} = 2$ accounts for the space-charge recombination current (Fig. 3.7).

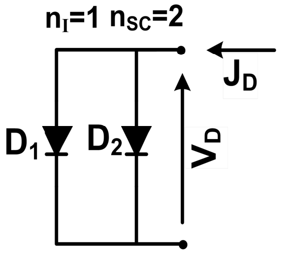

Figure 3.7: Compact model for single-crystal CIGS solar cells.

Fig. 3.8 shows the perfect match between numerical simulations and the two-diode compact model for various bulk trap densities in the CIGS (N_B) in the case of syngle-crystal cell. The saturation currents of the two diodes are shown as a function of N_B in Fig. 3.9. The space-charge recombination saturation current J_{02} duly scales linearly with defect density; on the other hand, the ideal diode current J_{01} shows the transition between a short-base diode behavior at low N_B, where the current is nearly independent of the electron diffusion length (hence of N_B), to a long-base diode behavior at large N_B, where J_{01} grows with N_B due to shortening of the diffusion length.

The presence of defect-rich grain boundaries alters the picture with respect to the single-crystal case, the valence band discontinuity at the GB (ΔE_V) playing a key role. For $\Delta E_V = 0.4$ eV, the large valence band offset makes the semiconductor nearly intrinsic at the GB, and keeps holes away from the GB, thus locally inhibiting recombination via the interface defects. The conduction band dip caused by the charged interface donors (see Fig. 3.2) results in some channeling of the electron current along the GB at low bias; however, at high bias the current is almost uniformly distributed

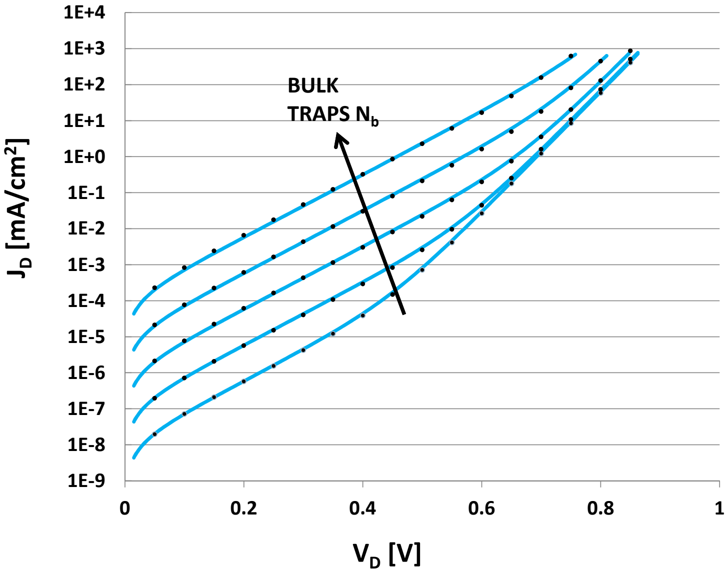

Figure 3.8: Dark I-V curves for the single-crystal cell (no GBs), with different bulk defect densities N$_B$ (10^{12}, 10^{13}, 10^{14}, 10^{15}, 10^{16} cm^{-3}) . The dots are numerical simulation results, the solid lines are obtained with the two-diode compact model.

along the direction orthogonal to the GB. Consequently, the dark I-V curve is only marginally altered with respect to the single-crystal cell. Therefore, the two-diode compact model described above is still valid. The situation is dramatically different when ΔEV = 0. Here the band dip caused by the GB defects (Fig. 3.2) results in a much enhanced channeling of the current along the GB, as shown in the maps of Fig. 3.10. This remarkable difference is evident in Fig. 3.11 that shows the dark current of the cell with ΔEV = 0 (solid line), together with the electron current flowing outside the GB just below the CdS/CIGS interface (dots), and the difference between the two (dashed line). At moderate and high bias all of the electron current injected by the CdS cathode flows along the GB. Due to the large injected electron concentration, and since the GB is depleted of holes by the band dip caused by interface defects, high-injection conditions are reached quite early at the GB, with the dark I-V curve showing the typical n_{HI} = 2 ideality factor beyond V_D = 0.5 V. A compact model physically representative of the cell with $\Delta E_V = 0$ at the GB must therefore include:

1. a diode with ideality factor n_I = 1 describing the ideal current flowing outside the GB (dots in Fig. 3.11);
2. a diode with n_{SC} = 2 describing the space-charge recombination current flowing outside the GB (dots in Fig. 3.11);
3. a diode with ideality factor n_{GB} = 1 describing the ideal current component flowing along the GB (dashed line in Fig. 3.11); this diode must dominate the GB current at low-to-moderate bias (below about 0.5 V in Fig. 3.11);
4. a diode with ideality factor n_{HI} = 2 describing the high-injection current flowing along the GB (dashed line in Fig. 3.11); this diode must dominate the GB current at moderate-to-high bias (above about 0.5 V in Fig. 3.11).

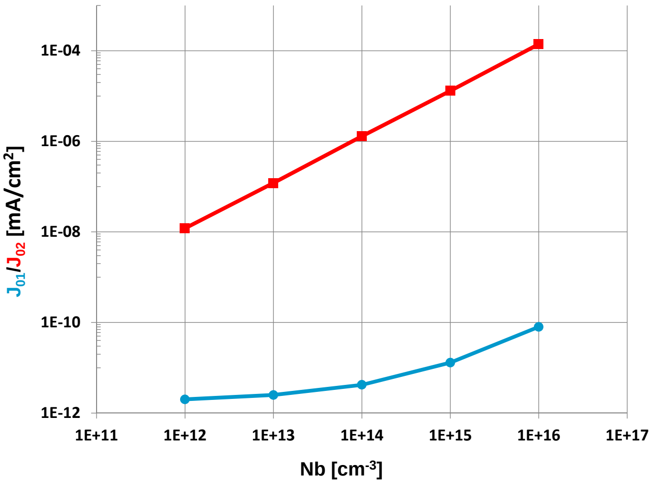

Figure 3.9: Two-diode compact model parameters J_{01} (circles) and J_{02} (squares) for the fit of Fig. 3.8, as a function of bulk trap density.

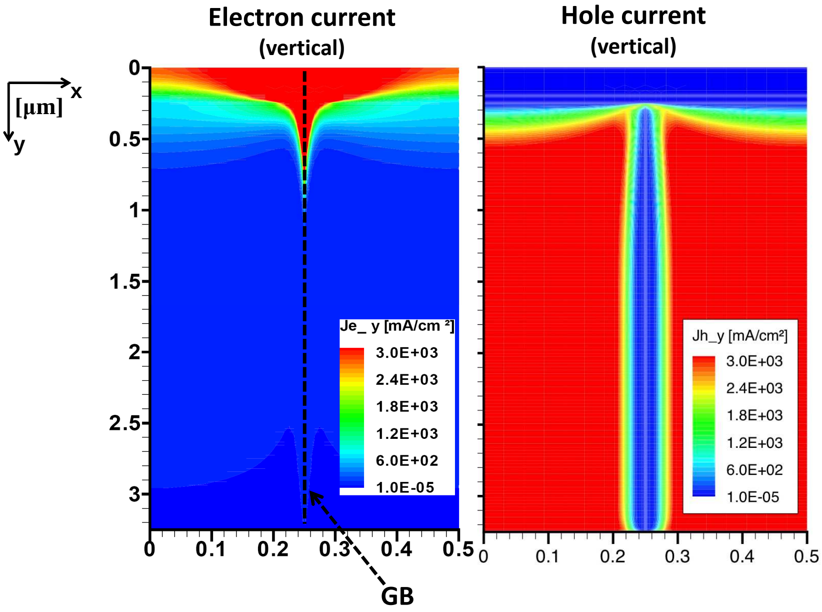

Figure 3.10: Electron and hole current density map for a cell with $N_I = 2{\cdot}10^{12}$ cm^{-2} defects at the grain boundary and $N_B = 10^{14}$ cm^{-3} in the grain interior. ΔEV = 0. V_D = 0.8 V.

The implementation of this model is a parallel connection of diodes (1) and (2) (see Fig. 3.12) with a voltage-controlled current source $I_{3-4}(V_D)$ accounting for the current components (3) and (4):

$$I_{3-4}(V_D) = \left(I_3(V_D)^{-1} + I_4(V_D)^{-1}\right)^{-1}. \tag{3.1}$$

This amounts to a 4-parameter model, the parameters being the saturation currents of diodes (1)-(4).

Fig. 3.13 shows the perfect match between the simulations and the four-diode compact model for various bulk trap densities in the CIGS (N_B). In this case the trap density at the GB is kept constant, therefore the parameters J_{03} and J_{04} relative to

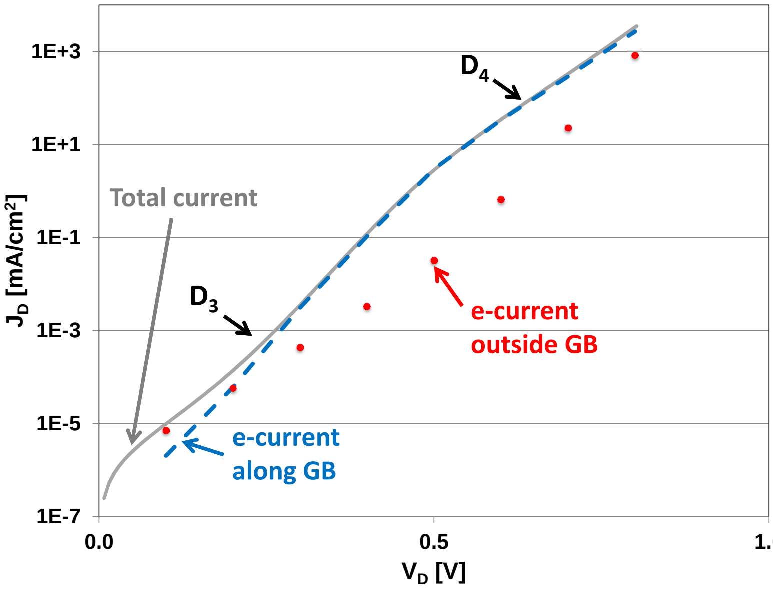

Figure 3.11: Solid line: dark current characteristics for a cell with $N_I = 2{\cdot}10^{12}cm^{-2}$ defects at the grain boundary, ΔEV = 0, and $N_B = 10^{14}$ cm^{-3}. Dots: electron current flowing outside the GB just below the CdS/CIGS interface. Dashed line: electron current flowing along the GB just below the CdS/CIGS interface.

the polycrystalline model are almost constant ($J_{03} \cong 3{\cdot}10^{-8}$ mA/cm^{-2}, $J_{04} \cong 3{\cdot}10^{-4}$ mA/cm^{-2}). According to the previous discussion, the first two parameters J_{01} and J_{02} that take into account for the different bulk trap densities in Fig. 3.13.

Fig. 3.14 shows the perfect match between the simulations and the four-diode compact model for different values of GB trap densities in the CIGS (Nit). The polycrystalline parameters J_{03} and J_{04} take into account for the the different GB trap densities in Fig. 3.14. The trend of these latter parameters is reported in Fig. 3.15 as a function of the GB trap density Nit.

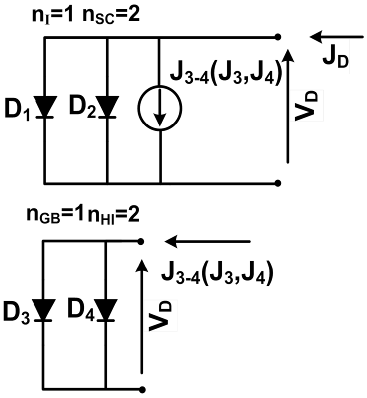
n_I=1 n_SC=2
J_D
J_3-4(J_3,J_4)
D_1
D_2
V_D
n_GB=1 n_HI=2
J_3-4(J_3,J_4)
D_3
D_4
V_D

Figure 3.12: Compact model for polycrystalline CIGS solar cells.

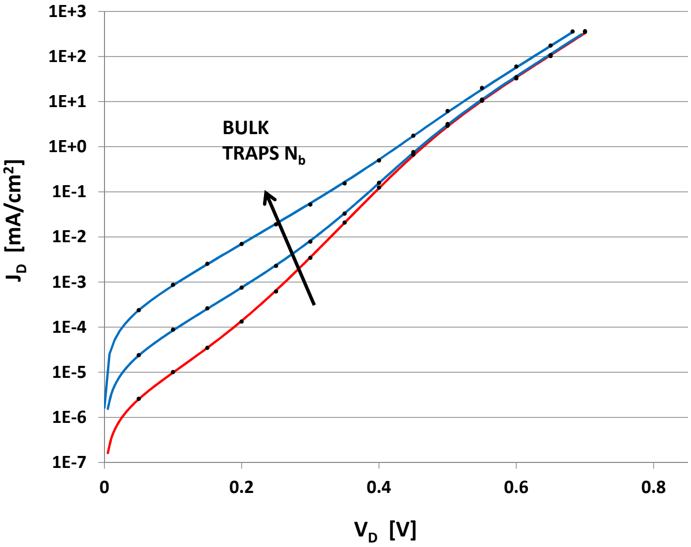

Figure 3.13: Dark current characteristics for a cell with $N_I = 2{\cdot}10^{12} cm^{-2}$ defects at the grain boundary; ΔEV = 0; $N_B = 10^{14}, 10^{15}, 10^{16}$ cm^{-3}. Solid line: numerical simulation. Dots: 4-diode compact model.

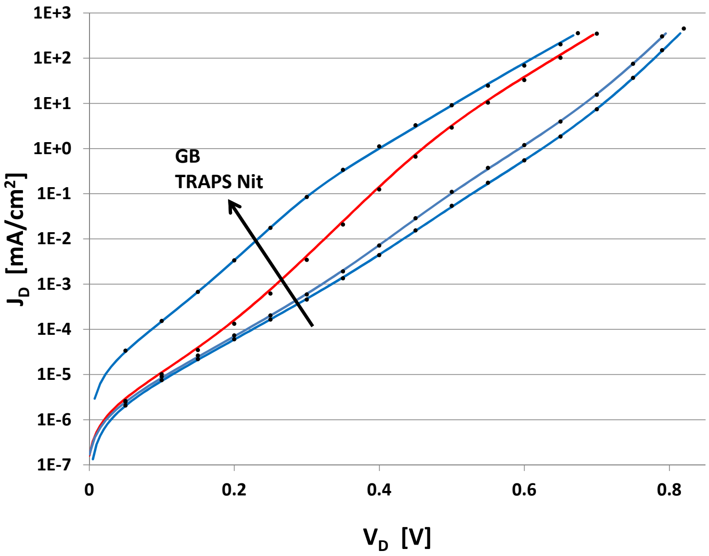

Figure 3.14: Dark current characteristics for a cell with N_I = $2{\cdot}10^{11}$, $4{\cdot}10^{11}$, $2{\cdot}10^{12}$, $4{\cdot}10^{12}$ cm^{-2} defects at the grain boundary; ΔEV = 0; N_B = 10^{14} cm^{-3}. Solid line: numerical simulation. Dots: 4-diode compact model.

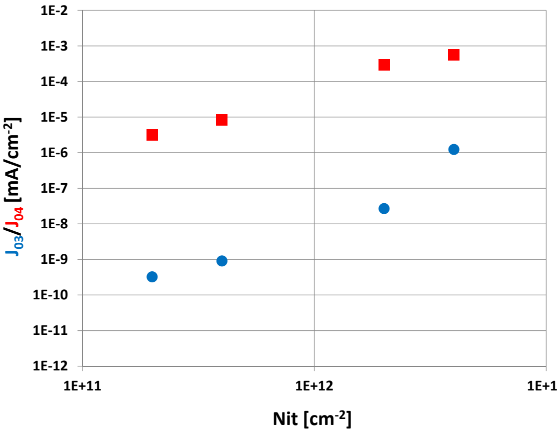

Figure 3.15: Four-diode compact model parameters J_{03} (circles) and J_{04} (squares) for the fit of Fig. 3.14, as a function of GB trap density.

3.3 Numerical simulation of damp heat degradation

Long-term reliability is obviously a key factor for the success of any solar cell technology. In particular, damp heat (e.g., 85 °C / 85% RH) is observed to be a critical condition for the long-term cell degradation. A numerical simulation model such as the one we developed can be usefully employed in this kind of investigation. As an example, we consider the change of defects distribution brought about by damp heat stress, as reported in [20] based on admittance spectroscopy measurements. Two defect are identified in [20]: N_1 is an interface defect undergoing activation energy increase during the stress, but not observed to influence the cell degradation, while N_2 is a bulk defect whose density and energy both increase upon stressing. We simulated the pre- and post-stress defect distribution of Fig. 3.16, as reported in [20], and obtained the cell performance parameters shown in Tab. 3.2, in qualitative agreement with published experimental observations.

	Pre-stress	**Post-stress**
V_{OC} [V]	0.641	0.613
J_{SC} [mA/cm^2]	26.3	24.7
Fill Factor [%]	71.9	70.1
Efficiency [%]	12.1	10.6

Table 3.2: Damp heat simulation results.

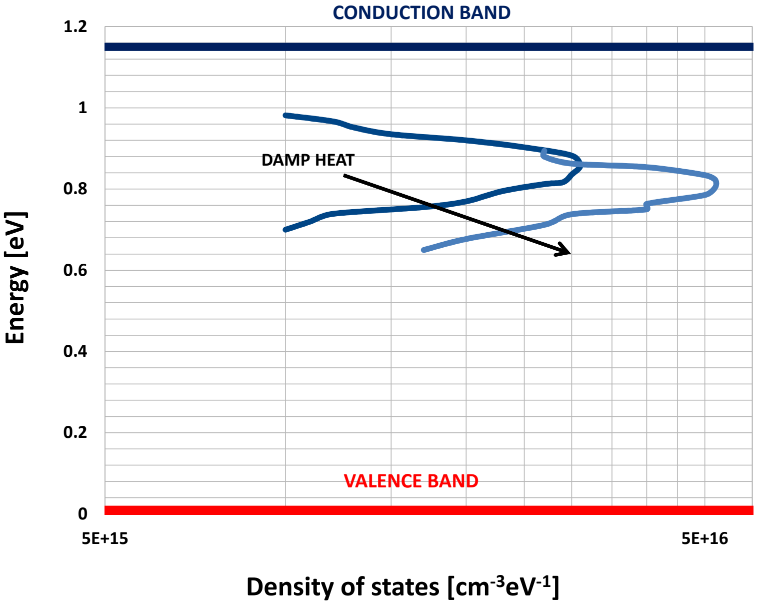

Figure 3.16: Pre- and post-stress defect distribution in the bulk of the CIGS absorber for the simulation of damp heat degradation ([20]).

3.4 Summary

We showed results of numerical as well as compact modeling of CIGS thin-film solar cells. The presence of defect-rich grain boundaries with possible band-gap modifications is a specific feature of these cells that must be accounted for in any physics-based model. We have used our numerical simulations as a benchmark to develop a simple, physics-based compact model of the behavior of the cell in the dark. While the single-crystal structure behavior can be accurately described by a standard two-diode model, when grain boundaries are present and active a four-diode model is required for a good match of the numerical simulation results.

We also simulated the modification of trap distribution N2 ([20]) taking into account for cell degradation under damp heat stress conditions.

Chapter 4

ZnMgO buffer layer

The traditional CIGS solar cell structure has, from top to bottom, a ZnO transparent contact layer, an n-doped CdS buffer layer, a p-doped CIGS absorber layer, and a backside metal (Mo) contact sitting on a soda lime glass or flexible substrate. The presence of toxic Cadmium poses environmental concerns that prompted research efforts aimed at replacing the CdS buffer with Cd-free layers [21, 22]. In this respect, ZnMgO has proven to be a suitable replacement for CdS, due to its wide bandgap (i.e., low absorption) and convenient band alignment with the CIGS absorber. When designing the cell window layer, some of the factors that must be reckoned with are:

1. transparency to the solar spectrum;
2. thickness, electron concentration and mobility;
3. band alignment with the underlying buffer or absorber, also in connection with the presence of interface defects.

While band alignment has been discussed before [21, 23], very little can be found on factors (1) and (2), their correlation, and combined effects with (3). In particular, data on carrier density and mobility (hence, resistivity) of ZnMgO layers are very scarce and widely dispersed. The cell's electrostatics is obviously a function, among other factors, of window layer thickness and electron concentration; the thickness also influences transparency, not only through absorption (which is generally neglected, particularly for relatively large Mg content) but due to reflection at the air/ZnMgO and ZnMgO/CIGS interfaces, a commonly overlooked phenomenon that becomes significant when the layer thickness is reduced to limit the series resistance. The aim of this chapter is therefore to provide theoretical indications for Cd-free CIGS solar cell design and manufacturing by showing results of numerical simulations of cells with varying $Zn_{1-x}Mg_xO$ bandgap (i.e., different Mg content x), thickness, and conductivity, with and without defects at the $Zn_{1-x}Mg_xO$/CIGS interface. These indications are meant to support the development of a novel manufacturing technology for CIGS solar cells under way at CNR-IMEM, Parma, Italy.

4.1 Numerical model

Simulations are performed using the Synopsys Sentaurus suite. The cell behavior in the dark is described by the Poisson, electron and hole continuity, and drift-diffusion equations. Unlike most simulations found in the literature, our model of the illuminated cell (standard AM1.5D solar spectrum) features a transfer matrix approach for the calculation of light propagation: this approach accounts for the effects of reflection at the interfaces between adjacent layers, a commonly overlooked effect that can significantly impact the cell efficiency. The characteristics of the CIGS absorber can be found in chapter 3 (except that here we use a 2 μm-thick absorber); since grain boundary effects have been treated in chapter 3 and here we focus on the window layer design, in this work we consider for simplicity the case of a single-crystal cell. The first design parameter to consider for the $Zn_{1-x}Mg_xO$ window layer is the Mg concentration x, since its bandgap is linearly increasing with x [24]. Larger bandgap means smaller absorption loss: we have calculated that with $x = 0.19$ less than 1% of the AM1.5D radiation is absorbed by $Zn_{1-x}Mg_xO$, so for x $\geq$ 0.19 we can confidently neglect this source of efficiency loss and consider the layer transparent. The $Zn_{1-x}Mg_xO$ bandgap on the other hand has a great impact in terms of band alignment and therefore of collection efficiency [21, 25, 23]. In this study we focus on two values: $x = 0.19$ and $x = 0.36$.

4.2 Simulation results

4.2.1 ZnMgO thickness and doping

In this subsection we consider the ZnMgO/CIGS heterointerface to be ideal, i.e., without traps.

The $Zn_{1-x}Mg_xO$ thickness t_W impacts the external quantum efficiency due to interference between waves reflected at the air/ZnMgO and ZnMgO/CIGS interfaces: the total reflection loss is therefore dependent on t_W, as shown in Fig. 4.1. This effect is accounted for in our simulations. Together with electron density n_W (and mobility μ_W), t_W also contributes to determining the electrostatics and current transport. Therefore, it must be investigated which combinations of x, t_W and n_W result in better cell efficiency.

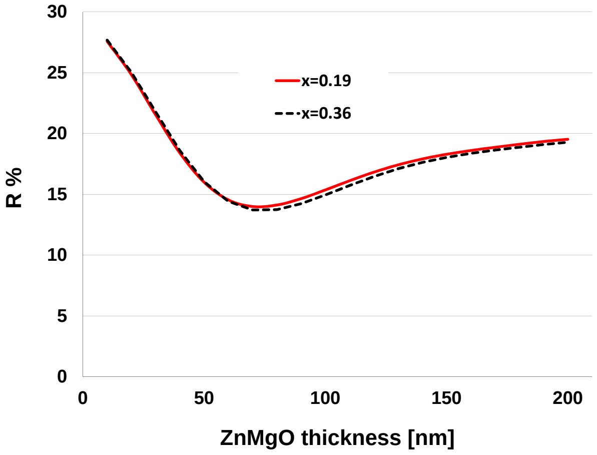

Figure 4.1: Cell reflectivity vs. window layer thickness.

Fig. 4.2 shows the equilibrium band diagram for a cell with $x = 0.36$, $t_W = 80$ nm, and different values of n_W: the very wide range of n_W values is consistent with what can be found in (or inferred from) the literature (compare for instance [26] and [27]). In these simulations we use a constant electron mobility in the ZnMgO, $\mu_W = 10$ cm^2/(Vs). Moving from low to high n_W the $Zn_{1-x}Mg_xO$ goes from full depletion to almost total neutrality, while the surface of the p-CIGS absorber gets depleted more and more by the cathode charge. This obviously has a big influence on the cell behavior, as will be shown below.

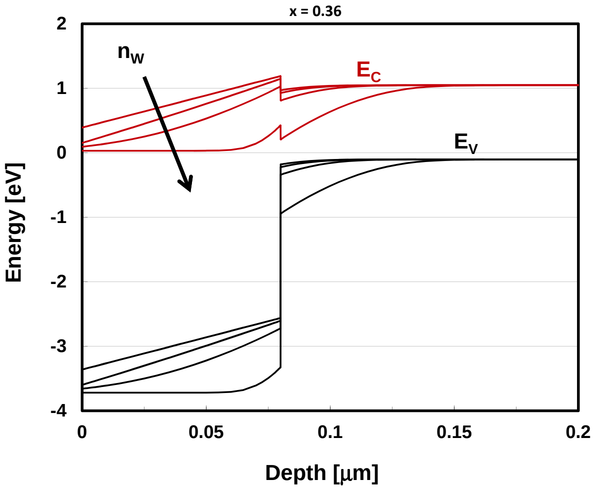

Figure 4.2: Band diagram for the $Zn_{1-x}Mg_xO$/CIGS interface. x = 0.36, t_W = 80 nm. The arrow indicates increasing values of n_W: 10^{12}, 10^{16}, 10^{17}, 10^{18} cm^{-3}.

Fig. 4.3 shows that the cell's short-circuit current J_{SC} has opposite dependence on t_W, depending on the electron concentration, n_W. Since the open-circuit voltage V_{OC} (Fig. 4.4) does not change much, this reflects directly on the behavior of the cell's efficiency in Fig. 4.5. For large values of n_W (like $n_W = 10^{18}$ cm^{-3} in figs. 4.3 and 4.5) the band alignment favors electron injection into the cathode (Fig. 4.2), and J_{SC} and η increase with t_W because of reduced reflection loss (Fig. 4.1), with a tendency to saturate or slightly decrease beyond t_W = 80 nm, possibly due to the reflectivity increase (Fig. 4.1); on the other hand, when n_W is low ($n_W = 10^{12}$ cm^{-3} in figs. 4.3 and 4.5) and the window layer is depleted (Fig. 4.2) the band alignment is such that electrons tend to be blocked before reaching the cathode, all the more so as the ZnMgO layer gets thicker, and both J_{SC} and η are degraded.

The importance of the band alignment on the overall cell behavior is confirmed by figs. 4.6 and 4.7, showing J_{SC} and η, respectively, as a function of $Zn_{1-x}Mg_xO$

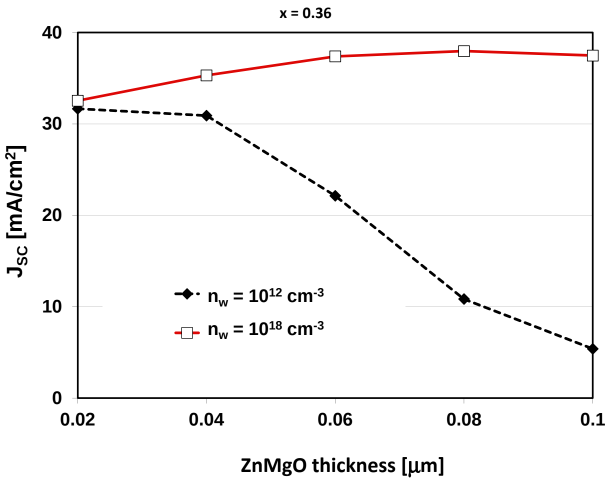

Figure 4.3: Short-circuit current vs. $Zn_{1-x}Mg_xO$ thickness for x = 0.36, and for two values of n_W, the electron concentration in the $Zn_{1-x}Mg_xO$.

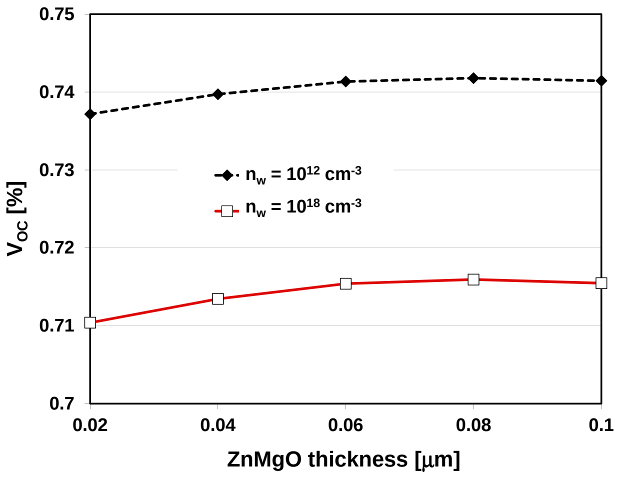

Figure 4.4: Open circuit voltage vs. $Zn_{1-x}Mg_xO$ thickness for x = 0.36, and for two values of n_W, the electron concentration in the $Zn_{1-x}Mg_xO$.

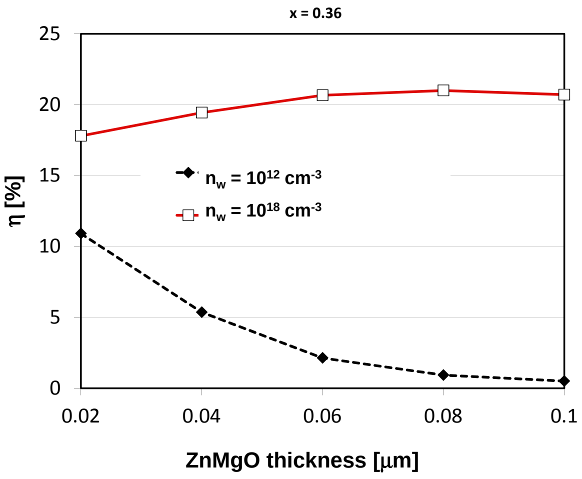

Figure 4.5: Cell efficiency vs. $Zn_{1-x}Mg_xO$ thickness for $x = 0.36$, and for two values of n_W, the electron concentration in the $Zn_{1-x}Mg_xO$.

window layer thickness, for the case of $x = 0.19$. By reducing the Mg content from 36% to 19%, the bandgap of $Zn_{1-x}Mg_xO$ shrinks from 3.75 eV to 3.49 eV, while the conduction band offset, which represents a barrier to electron flow from the absorber to the cathode, drops from 0.22 eV to 0.04 eV. A comparison of Fig. 4.6 with Fig. 4.3, and Fig. 4.7 with Fig. 4.5, shows that the reduced conduction band offset significantly weakens the importance of the electron density n_W and, for the lower densities, the dependence on the thickness t_W.

If we fix the $Zn_{1-x}Mg_xO$ thickness at t_W = 80 nm, which yields the peak efficiencies (figs. 4.5 and 4.7), and vary its electron concentration n_W, we observe the results of Fig. 4.8. As noted above, for $x = 0.36$ low electron densities result in unfavorable band alignment, and only for $n_W \geq 10^{18}$ cm^{-3} does the efficiency attain satisfactory values. On the other hand, for $x = 0.19$, the lower conduction band offset between $Zn_{1-x}Mg_xO$ and CIGS makes the band alignment, shown in Fig. 4.9, more forgiving even at low or very low electron concentrations, and η decreases much more gently for decreasing n_W. For $n_W \geq 10^{19}$ cm^{-3}, yielding degenerate $Zn_{1-x}Mg_xO$, there is no more dependence of η on x, due to absence of a significant barrier to electron flow.

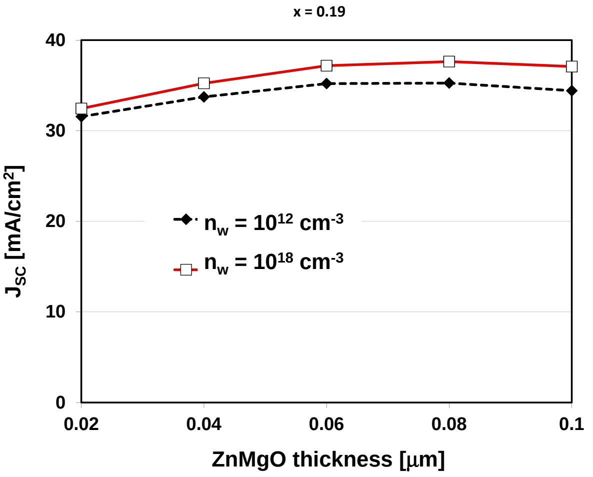

Figure 4.6: Short-circuit current vs. Zn$_{1-x}$Mg$_x$O thickness for x = 0.19, and for two values of n$_W$, the electron concentration in the Zn$_{1-x}$Mg$_x$O.

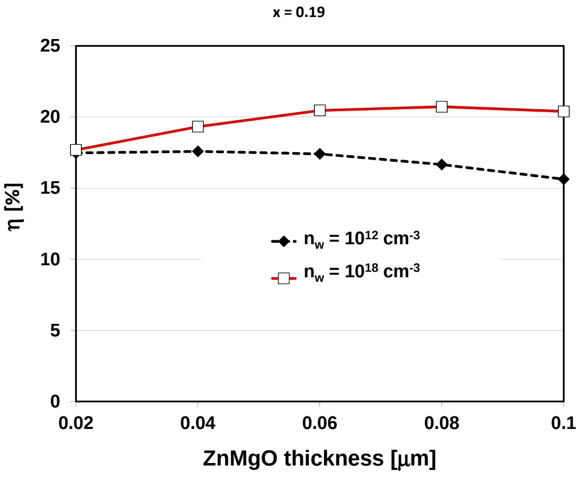

Figure 4.7: Cell efficiency vs. Zn$_{1-x}$Mg$_x$O thickness for x = 0.19, and for two values of n$_W$, the electron concentration in the Zn$_{1-x}$Mg$_x$O.

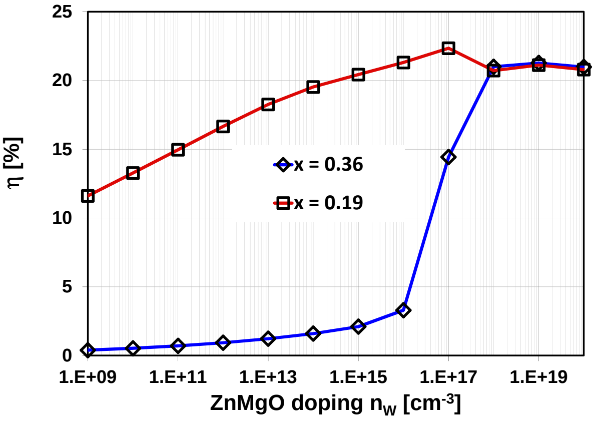

Figure 4.8: Cell efficiency vs. $Zn_{1-x}Mg_xO$ electron concentration.

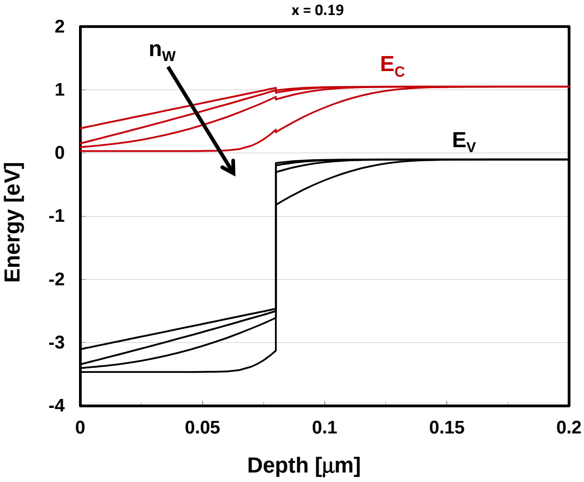

Figure 4.9: Band diagram for the $Zn_{1-x}Mg_xO$/CIGS interface. $x = 0.19$, t_W = 80 nm. The arrow indicates increasing values of n_W: 10^{12}, 10^{16}, 10^{17}, 10^{18} cm^{-3}.

4.2.2 Interface states at ZnMgO/CIGS heterostructure

The presence of interface traps between the $Zn_{1-x}Mg_xO$ window layer and the CIGS absorber quantitatively alters the picture as described so far. Tab. 4.1 summarizes the trap parameters used in our simulations.

Type	**Density N_{IT}**	**Energy**	**Capture cross-section**
Donor	10^{11} to 10^{13} cm^{-2}	CIGS midgap	10^{-15} cm^2

Table 4.1: $Zn_{1-x}Mg_xO$/CIGS interface trap parameters.

Figs. 4.10 to 4.13 summarize the cell performance in the presence of interface traps with concentrations ranging from 10^{11} to 10^{13} cm^{-2}, as a function of $Zn_{1-x}Mg_xO$ electron density n_W. We focused on the case of $x = 0.19$ since, as shown by Fig. 4.8, under no doping condition does the structure with $x = 0.36$ offer any advantage over that with $x = 0.19$, while it is markedly inferior for low to moderate $Zn_{1-x}Mg_xO$ doping.

The structure with the lowest trap density ($N_{IT} = 10^{11}$ cm^{-2}) does not show any appreciable difference from the case of ideal trap-free interface. On the other hand, $N_{IT} = 10^{12}$ cm^{-2} is enough to produce a marked degradation of the cell's performance. While the short-circuit current (Fig. 4.10) is unaffected by this trap concentration, the open-circuit voltage (Fig. 4.11), as expected, is significantly degraded by the increase of non-radiative recombination. Together with some reduction of the fill factor (Fig. 4.12), the decrease of V_{OC} causes significant efficiency loss (Fig. 4.13). This trend is accentuated for $N_{IT} = 10^{13}$ cm^{-2}. It should be noticed that for $n_W \geq 10^{18}$ cm^{-3} the presence of trap does not alter the cell's behavior, no matter what is the trap concentration. As shown in Fig. 4.9, with heavily doped $Zn_{1-x}Mg_xO$ layer the band alignment is such that the interface traps (energetically located at the middle of the CIGS bandgap) are far below the Fermi level; consequently, they are always filled with electrons, and therefore inactive.

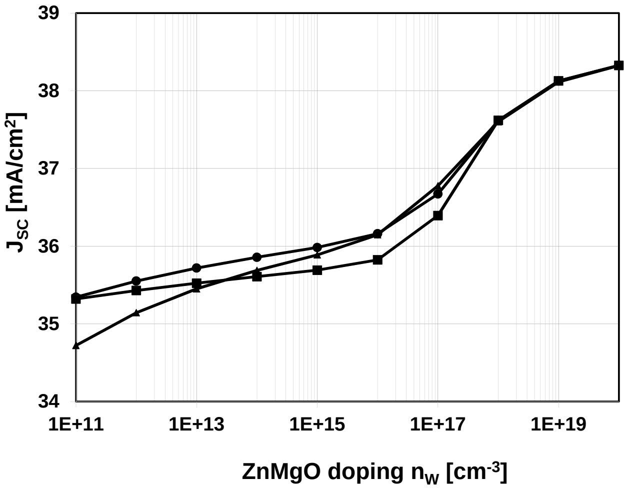

Figure 4.10: Short-circuit current vs $Zn_{1-x}Mg_xO$ electron concentration. $x = 0.19$. $N_{IT} = 10^{11}$ cm^{-2} (squares), $N_{IT} = 10^{12}$ cm^{-2} (circles), $N_{IT} = 10^{13}$ cm^{-2} (triangles).

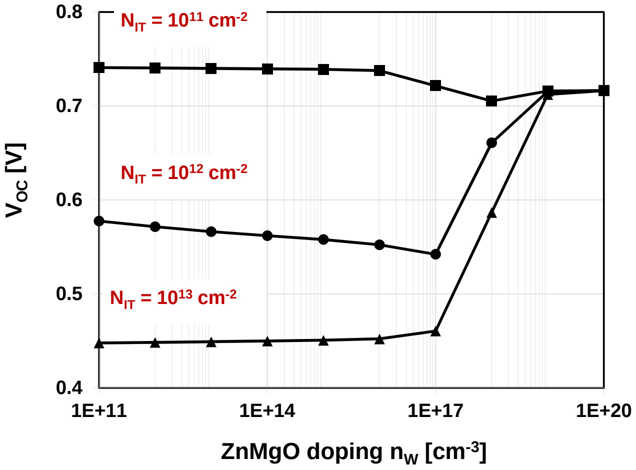

Figure 4.11: Open circuit voltage vs $Zn_{1-x}Mg_xO$ electron concentration. $x = 0.19$. $N_{IT} = 10^{11}$ cm^{-2} (squares), $N_{IT} = 10^{12}$ cm^{-2} (circles), $N_{IT} = 10^{13}$ cm^{-2} (triangles).

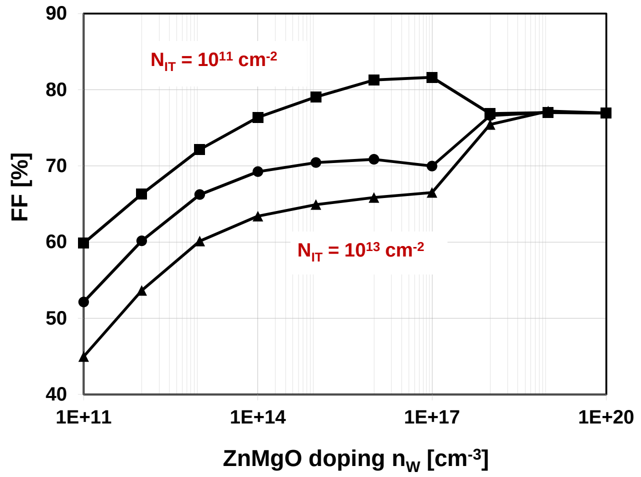

Figure 4.12: Fill factor vs $Zn_{1-x}Mg_xO$ electron concentration. $x = 0.19$. $N_{IT}= 10^{11}$ cm^{-2} (squares), $N_{IT}= 10^{12}$ cm^{-2} (circles), $N_{IT}= 10^{13}$ cm^{-2} (triangles).

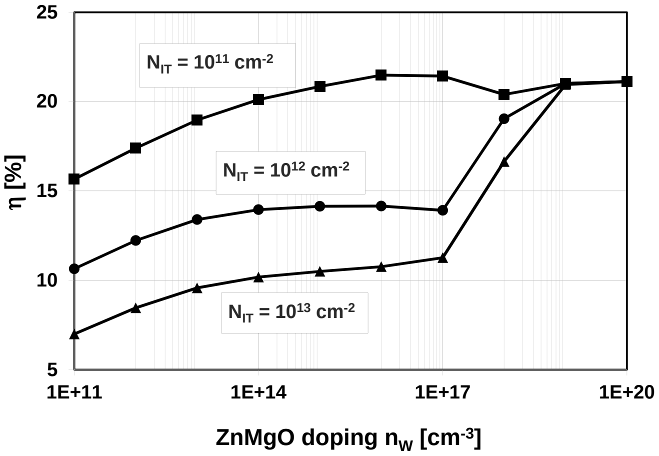

Figure 4.13: Cell efficiency vs $Zn_{1-x}Mg_xO$ electron concentration. $x = 0.19$. $N_{IT}=$ 10^{11} cm^{-2} (squares), $N_{IT}= 10^{12}$ cm^{-2} (circles), $N_{IT}= 10^{13}$ cm^{-2} (triangles).

4.3 Summary

In this chapter we developed numerical simulations of Cd-free CIGS solar cells, and specifically studied the impact of thickness, Mg content and doping of the $Zn_{1-x}Mg_xO$ buffer layer, with and without interface states at the $Zn_{1-x}Mg_xO$/CIGS interface. We have shown that, for the case of ideal $Zn_{1-x}Mg_xO$/CIGS interface, large Mg concentration ($x = 0.36$) necessitates nearly degenerate or degenerate $Zn_{1-x}Mg_xO$ to achieve good efficiency, while at lower concentration ($x = 0.19$) the electron concentration in the $Zn_{1-x}Mg_xO$ is much less critical. The thickness of the $Zn_{1-x}Mg_xO$ layer should also be tailored based on a careful analysis of the total reflection of the incident light. In the presence of non-ideal $Zn_{1-x}Mg_xO$/CIGS interface, increasing interface trap densities result, as expected, in open-circuit voltage and, consequently, efficiency degradation. Heavy doping of the $Zn_{1-x}Mg_xO$ layer ($n_W \geq 10^{18}$ cm^{-3}) results in full occupation, and inactivation, of the mid-gap traps.

Chapter 5

Modeling of CdTe Solar Cells

Thin-film solar cells based on CIGS or CdTe absorbers have been studied in research laboratories for at least 20 years, but only recently entered the phase of industrial production [1]. While still lagging behind their Si-based competitors in terms of efficiency and dollars/Watt, these technologies are poised to conquer increasing market shares, and perhaps even market dominance. However, for the time being CdTe solar cells still underperform compared with theoretical limits and even with CIGS cells [3], and in spite of a relatively long history of research and development, there is still room and need for better understanding of the physics underpinning the photovoltaic performance of CdTe cells and modules.

One difficulty lies in the fact that while single crystal materials used in traditional (silicon) and high efficiency tandem (GaAs-based) solar cells are well-known and fully characterized, poly-crystalline materials used in thin-film solar cells show widely varying characteristics depending on growth/deposition process and conditions; the poly-crystalline nature of the absorber is itself an obstacle along the path to full understanding of the cell behavior, and often the device is studied by simulating an equivalent single-crystal solar cell where the material parameters, such as carrier lifetimes, are modified to give a reasonable match of the experiments. This approach has the major advantage of allowing a one-dimensional description of the cell, and the use of efficient and widespread one-dimensional simulation tools like SCAPS [4].

However, the actual current transport mechanisms, which are necessarily affected by the presence of grain boundaries, cannot be investigated using this approximation; consequently, this aspect of device design and optimization is neglected.
In this study we develop a two-dimensional numerical model of a CdTe solar cell and specifically address the simulation of grain boundaries and their effect on current transport and, ultimately, on the photovoltaic figures of merit.

5.1 Numerical model

Simulations are performed using the Synopsys Sentaurus suite. The electrical cell behavior is simulated using the drift-diffusion model, with the Poisson equation describing the electrostatic problem and the occupation probability following the Fermi statistics. Each material is optically described by its wavelength-dependent complex refractive index, the real part of which is the refractive index and the imaginary part is the extinction coefficient determining light absorption. Since the optical properties of the grain boundary regions are not known, the complex refractive index of CdTe is considered to be constant throughout the whole absorber layer. The optical problem is therefore solved using the one-dimensional transfer matrix method, with the cell illuminated by the global AM1.5 spectrum. This method takes into account multiple reflections at the hetero-interfaces, and the anti-reflective properties of the first layers can be evaluated.
The main properties of the cell materials are summarized in Tab. 5.1.

Material	**Bandgap** [eV]	**Doping** [cm^{-3}]	χ [eV]	**Mobility** [cm^2/(Vs)]	**Lifetime** [s]
CdTe	1.5	p:10^{14}÷$7\cdot10^{14}$	4.5	e:100 h:25	e:$1.5\cdot10^{-9}$ p:$3\cdot10^{-9}$
CdS	2.4	n:10^{16}	4.6	e:320, h:40	e:10^{-9}, p:10^{-9}

Table 5.1: CdTe material parameters.

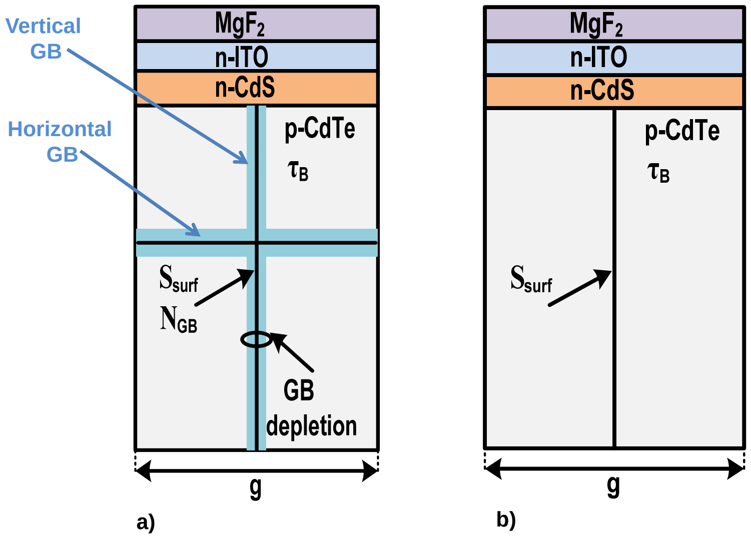

Figure 5.1: Schematic structure of the simulated CdTe solar cell. a) Model with charged vertical and horizontal grain boundaries. b) Partial model considering only a vertical neutral grain boundary.

Starting from the single-crystal CdTe solar cell, the model is modified to include grain boundaries (GBs), charge trapping and grain-to-grain transport. Both vertical and horizontal GBs are considered. At the grain boundaries we consider the presence of localized trap states and surface recombination. Both surface and bulk recombination follow the Shockley-Read-Hall (SRH) model, as determined by the effective carrier lifetimes in the bulk (Tab. 5.1) and by the surface recombination velocity at the GB, assumed to be 10^6 cm/s as suggested by surface studies [28]. The states at the GB are assumed to be substitutional Cl_{Te} donor defects coming from annealing in the presence of a source of chlorine ($CdCl_2$) [29]. This processing step is common to all the best CdTe solar cells. The activation energy of Cl_{Te} states is 350 meV (below the conduction band minimum) [30] and their concentration is in the range $10^{11} \div 5 \cdot 10^{11}$ cm^{-2}, yielding a downward band bending of $0.1 \div 0.8$ eV and a hole-depleted region of $100 \div 300$ nm across the GB, as observed experimentally [31]. The Cl_{Te}

states modify the system electrostatics based on their occupation state, but not the GB recombination, which is set by the fixed surface recombination velocity of 10^6 cm/s.

Part of the modeled structure is schematically shown in Fig. 5.1. The common process adopts a superstrate configuration, where the CdS buffer and the CdTe absorber are deposited on TCO-coated glass. In the record cells an antireflective (MgF) coating is also included.

5.2 Simulation results

5.2.1 Vertical grain boundaries

First we analyzed the impact of recombination at vertical GBs as a function of CdTe grain size (g) and doping. In these simulations, no horizontal GB are considered, i.e., the CdTe absorber layer is columnar, and Cl_{Te} states are absent, i.e., GBs are charge-neutral: the simulated structure, therefore, is that of Fig. 5.1b. Results are shown in Fig. 5.2. Increasing the grain size enhances the efficiency toward the single-crystal limit, due to reduced non-radiative recombination at the (neutral) GBs. The efficiency also increases with increasing acceptor concentration in the absorber: higher doping concentration reduces the diode's saturation current, hence increasing the open-circuit voltage (V_{OC}, Fig. 5.3). The expected decrease of the short-circuit current (J_{SC}, Fig. 5.4) with increasing doping is overcompensated by the improvement of V_{OC} and by the reduction of recombination at GBs. In fact, only for larger grain size, where the impact of GB recombination is less significant, does the case with higher doping show a reduction of short circuit current (see Fig. 5.4). The fill factor (Fig. 5.5) is the result of all the effects above mentioned.

The efficiency increase is consistent with the observed improvement of the cell performance after the recrystallization step, which is known to produce an increase of the grain size [29].

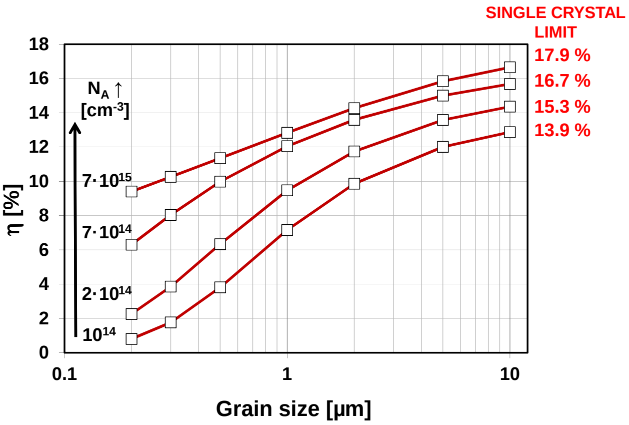

Figure 5.2: Impact of the grain size g (in the structure of Fig .5.1b) on the solar cell conversion efficiency η for different values of the CdTe doping density N_A.

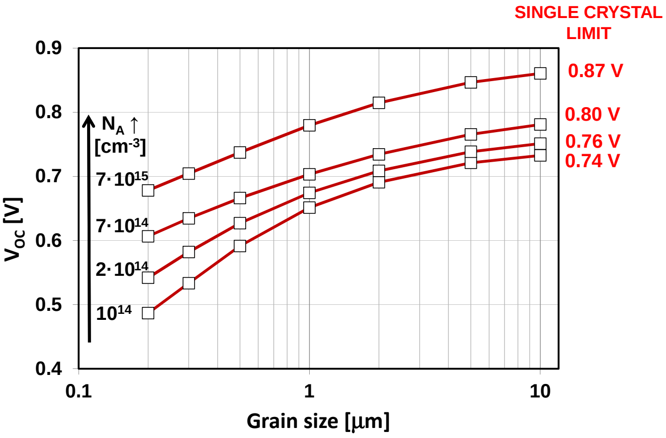

Figure 5.3: Impact of the grain size g (in the structure of Fig. 5.1b) on the solar cell open circuit voltage V_{OC} for different values of the CdTe doping density N_A.

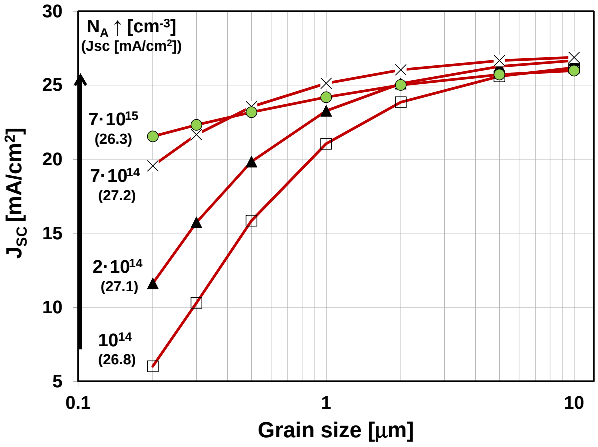

Figure 5.4: Impact of the grain size g (in the structure of Fig .5.1b) on the solar cell short circuit current J_{SC} for different values of the CdTe doping density N_A.

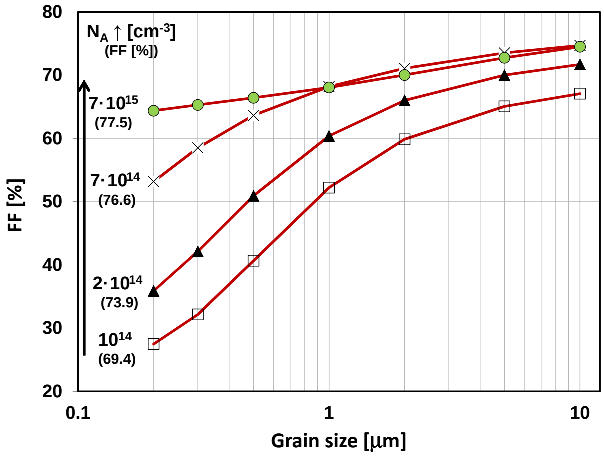

Figure 5.5: Impact of the grain size g (in the structure of Fig .5.1b) on the solar cell fill factor FF for different values of the CdTe doping density N_A.

In a second set of simulations, we considered the presence of the Cl_{Te} states at the GB. Using densities of Cl_{Te} states in the range 10^{11} to $5 \cdot 10^{11}$ cm^{-2} simulations show a downward band bending of $0.1 \div 0.8$ eV, and a hole-depleted region of $100 \div 300$ nm, as illustrated by Fig. 5.7 and observed experimentally by other groups [31]. This enhances electron collection at GBs by up to five times near the metallurgical junction [32]: Fig. 5.8 shows the vertical current density along a horizontal cut near the CdS/CdTe metallurgical junction. Introducing low densities of traps at GBs ($10^{11} \div 2 \cdot 10^{11}$ cm^{-2}) increases recombination due to the increased concentration of minority electrons; as the trap density becomes higher, though, the positively-charged GBs repel holes, and the recombination rate starts to decrease (Fig. 5.6). It should also be pointed out that, since the n-type doping of the CdS buffer layer pulls the Fermi level closer to the conduction band in the CdTe near the metallurgical junction, the Cl_{Te} donor states, located 350 meV below the conduction band minimum [30], get filled by electrons, thus becoming neutral close to the junction.

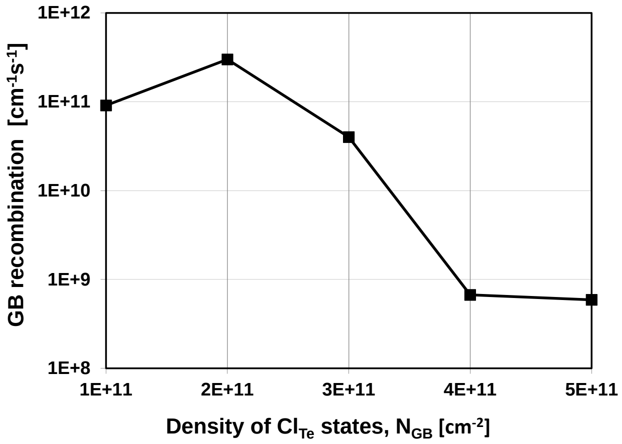

Figure 5.6: Surface recombination rate integrated along the grain boundary as a function of the density of Cl_{Te} states. $N_A = 7 \cdot 10^{15}$ cm^{-3}.

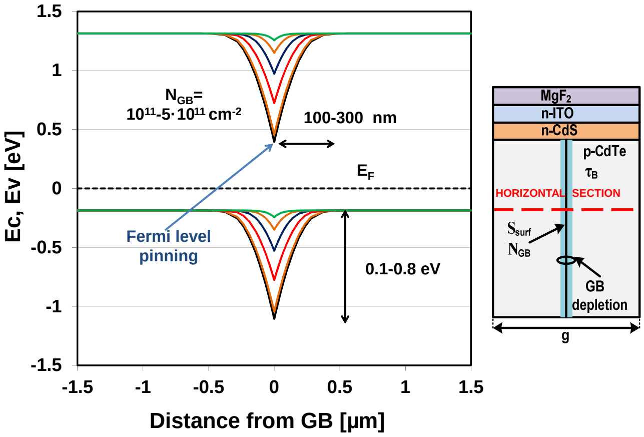

Figure 5.7: Band diagram near the (vertical) grain boundary, for different values of the density of Cl_{Te} states at the grain boundary. $N_A = 7 \cdot 10^{15}$ cm^{-3}.

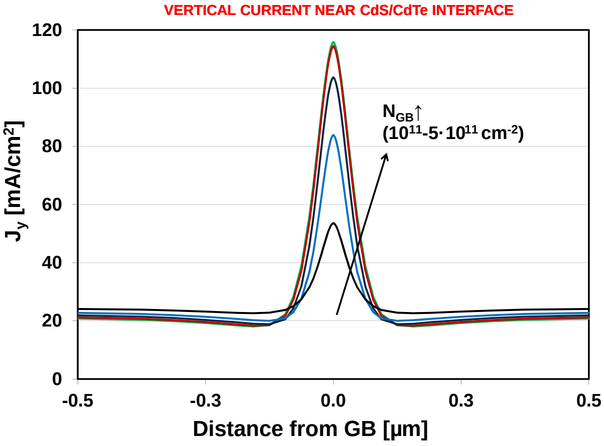

Figure 5.8: Vertical current distribution along a horizontal cut near the metallurgical junction in the presence of a vertical grain boundary, for different values of the density of Cl_{Te} states at the grain boundary (see Fig. 5.7). $N_A = 7 \cdot 10^{15}$ cm^{-3}.

5.2.2 Horizontal grain boundaries

As illustrated by Fig. 5.1a, we also simulated the presence of horizontal GBs, either neutral or decorated by Cl_{Te} donor states. While neutral GBs can easily be crossed by current, charged ones present a barrier to the hole current due to the spike in the valence band profile shown in Fig. 5.7. However, the cell can operate even in the presence of trap-decorated horizontal GBs. As shown by the current density map of Fig. 5.9, drawn under illumination at the maximum power point, while holes preferentially flow along the two columnar grains, the presence of the deep donor-decorated traps at the horizontal GBs does not prevent substantial current to flow across the horizontal GB. Under illumination, the photo-generated electrons are collected by the positively-charged GB: this lowers the potential of the GB and makes it less repulsive for holes, as shown by Fig. 5.10. The unit-area resistance of the charged GB decreases from tens of $k\Omega \cdot cm^2$ (at thermal equilibrium) to less than one tenth of $\Omega \cdot cm^2$, sufficiently low for substantial current to flow through. It can be noticed in Fig. 5.10 that the dip in the band profiles caused by the horizontal GB at equilibrium (a magnified picture of which is shown in Fig. 5.7) all but disappears when the cell is illuminated. The tendency of holes to populate the GBs under illuminated conditions is also illustrated by Figs. 5.11 and 5.12, showing hole concentrations along vertical and horizontal GBs: when the cell is operated under illumination at the maximum power point, the hole concentration along the GB is enhanced by several orders of magnitude with respect to equilibrium conditions.

Summarizing, we have shown that neither vertical nor horizontal donor-decorated grain boundaries hinder current conduction when the cell is illuminated.

Tab 5.2 reports some simulation results (compatible with published data [33]). If, from the baseline (ideal) single-crystal cell (case a), we move to a poly-crystalline cell with 1 μm grain size, no recrystallization step [34] (i.e., without Cl_{Te} donor states), and low acceptor doping (case b), the cell's performance degrades remarkably.

By increasing the acceptor concentration in the absorber (case c), the efficiency is significantly improved, largely thanks to higher V_{OC} and FF.

If we also include Cl_{Te} donor states (case d) - an effect of recrystallization in the presence of chlorine - the efficiency gets closer to the ideal value, due to larger J_{SC}

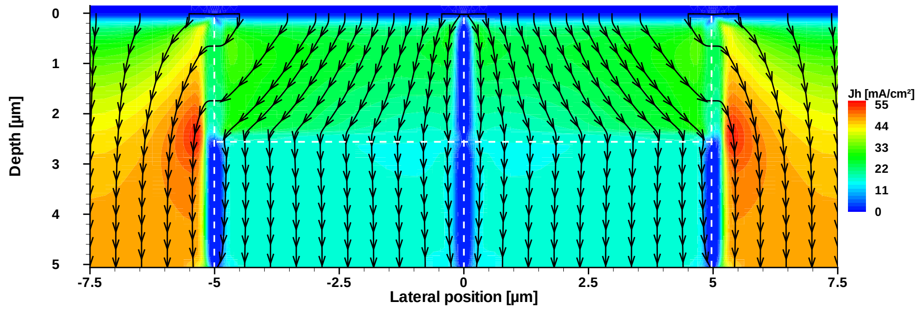

Figure 5.9: Hole current density map for the solar cell operating at its maximum power point (anode-cathode voltage: 0.675 V). The structure is composed by six grains: grain boundaries are indicated by dashed lines. The density of Cl_{Te} states at every grain boundary is $N_{GB} = 5 \cdot 10^{11}$ cm^{-2}, while the doping density of the CdTe is $N_A = 7 \cdot 10^{15}$ cm^{-3}.

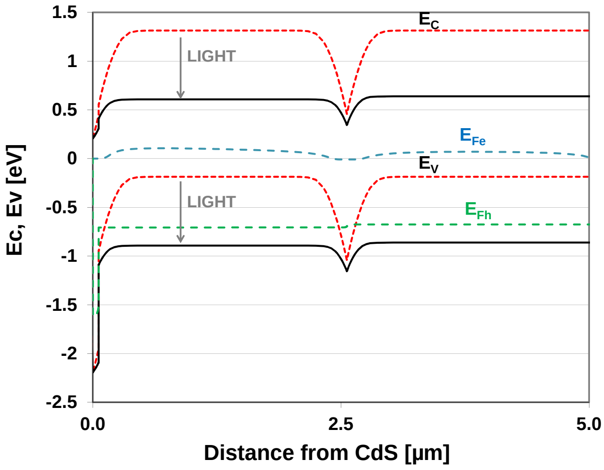

Figure 5.10: Band diagram along a vertical cut at lateral position = 5 μm in the structure in Fig. 5.9. Solid lines: maximum power point; dashed lines: thermal equilibrium.

and FF; the reason for the larger J_{SC} is explained by Fig. 5.8: the positively charged vertical GB attracts the electron current and collection efficiency is significantly im-

Case	**V_{OC}**	**J_{SC} [mA/cm^2]**	**FF %**	**η %**
a	0.88	26.3	77.5	17.9
b	0.67	23.3	60.4	9.5
c	0.78	24.2	68.0	12.8
d	0.80	25.7	72.7	15.8
e	0.85	26.7	75.9	17.1
f	0.86	27.3	73.0	17.1

Table 5.2: CdTe solar cell performance. a) Single-crystal, $N_A = 7\cdot10^{15}$ cm^{-3}. b) Columnar poly-crystalline cell (vertical grain boundaries only), g = 1 μm, no Cl_{Te} states, $N_A = 2\cdot10^{14}$ cm^{-3}. c) Columnar poly-crystalline cell (vertical grain boundaries only), g = 1 μm, no Cl_{Te} states, $N_A = 7\cdot 10^{15}$ cm^{-3}. d) Columnar poly-crystalline cell (vertical grain boundaries only), g = 1 μm, $N_{GB} = 5\cdot10^{11}$ cm^{-2}, $N_A = 7\cdot 10^{15}$ cm^{-3}. e) Columnar polycrystalline cell (vertical grain boundaries only), g = 5 μm, no Cl_{Te} states, $N_A = 7\cdot 10^{15}$ cm^{-3}. f) Columnar polycrystalline cell (vertical grain boundaries only), g = 5 μm, $N_{GB} = 5\cdot10^{11}$ cm^{-2}, $N_A = 7\cdot 10^{15}$ cm^{-3}. g) Vertical and horizontal GBs (structure of Fig. 5.9), $N_{GB} = 5\cdot10^{11}$ cm^{-2}, $N_A = 7 \cdot 10^{15}$ cm^{-3}.

proved.

If the grain size is increased from 1 μm to 5 μm (case e), (another known effect of the re-crystallization step), the V_{OC} is improved significantly due to smaller impact of GB recombination.

Including the Cl_{Te} donor states again (case f) results in a larger J_{SC} and efficiency exceeding 17%.

Finally, if we consider the structure of Fig. 5.9 (case g), the J_{SC} and FF decrease somewhat due to the presence of horizontal GBs, but thanks to the electron collection effect mentioned above, the cell's performance is only moderately affected.

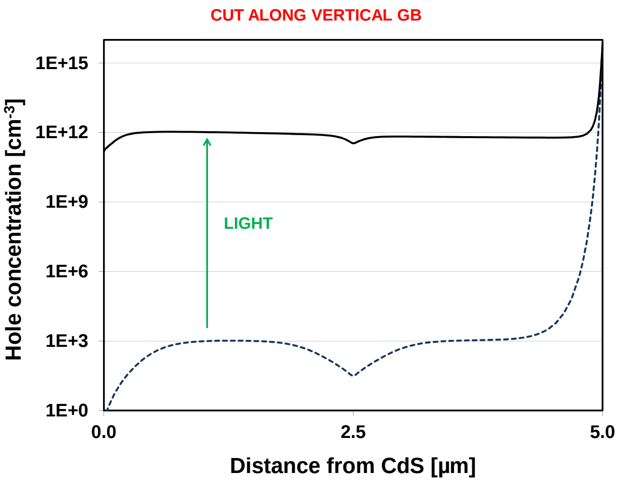

Figure 5.11: Hole concentration along a vertical cut at lateral position = 5 μm in the structure in Fig. 5.9. Solid line: maximum power point; dashed line: thermal equilibrium.

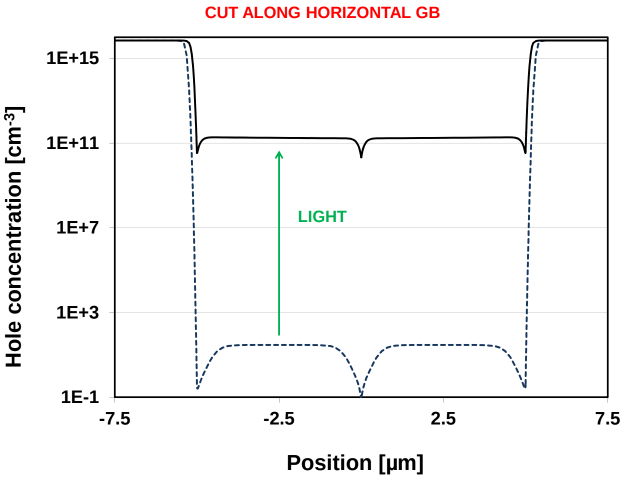

Figure 5.12: Hole concentration along a horizontal cut at depth = 2.5 μm (i.e., along the horizontal grain boundaries) in the structure in Fig 5.9. Solid line: maximum power point; dashed line: thermal equilibrium.

5.3 Summary

We have used two-dimensional numerical simulations to study the impact of vertical as well as horizontal grain boundaries in the absorber layer of CdTe solar cells. We considered the effect of absorber doping, grain size, and concentration of Cl_{Te} donor traps at the grain boundaries, a known by-product of re-crystallization in the presence of chlorine (a processing step used to increase grain size and yielding more efficient cells). Besides being consistent with known experimental results, such as the increase of efficiency with grain size and absorber acceptor density, our simulations indicate that:

- in a columnar absorber (i.e., one where only vertical grain boundaries exist) the presence of Cl_{Te} donor traps at the grain boundaries results in a dip in the band profiles that effectively serves as electron collector, increasing short-circuit current;
- while the same dip acts as a hole barrier and thus can be expected to block holes from flowing through the diode when horizontal grain boundaries are present, under illuminated conditions electron collection at the grain boundary reduces the dip enough to allow substantial hole flow, and the cell's performance is only moderately affected.

Chapter 6

Conclusions

This thesis presents modeling results of thin-film CIGS and CdTe solar cells with the goal to provide insight to the device physics and help a better understanding of the cell behavior.
The mathematical complexity and multidimensional nature of the physics governing these solar cells require in general that the problem be addressed numerically. In this work both numerical and analytical models are used, combining accuracy in describing arbitrary structures and complex transport mechanisms with the compactness and ease of integration into CAD tools of the latter. This helps bridging the gap between experimental observation of measurable quantities, e.g. current-voltage characteristic, and the knowledge of the real device physics, often difficult to understand simply by direct observation.

An analytical model for the short-circuit current of a thin-film solar cell has been developed. The validity of the model is proven over a large range of doping and deep state concentrations using numerical simulations. The reference structure for the validation is ZnO/CdS/CIGS; however, the model is valid for a wider range of thin-film solar cells. While other models oversimplificate the optics, the use of the complex tranfer matrix method in this model allows to account for optical behavior of the various layers and interfaces. Buffer and window layers have a small impact on the short circuit current, and constant optical generation can be assumed. The current in the absorber is obtained considering exponential generation and its contribute is increased with decreasing doping. From the transport analysis in the quasi-neutral region we see how increasing the diffusion length (lower trap density) the short circuit current can also be increased. A longer diffusion length allows higher doping in the absorber without a drastical decrease of the current, which is an advantage to obtain high open circuit voltage.

Numerical and compact modeling of CIGS thin-film solar cells has been developed. The presence of defect-rich grain boundaries with possible band-gap modifications is a specific feature of these cells that must be accounted for in any physics-based model. We have also used our numerical simulations as a benchmark to develop a simple, physics-based compact model of the behavior of the cell in the dark. While the single-crystal structure behavior can be accurately described by a standard two-diode model, when grain boundaries are present a four-diode model is required for a good match of the numerical simulation results.
A modification of trap distribution has been been simulated to take into account the cell degradation under damp heat stress conditions.

Numerical simulations have also been used to consider ZnMgO as an alternative window layer for Cd-free CIGS solar cells. The study included the impact of thickness, Mg content and doping of the ZnMgO buffer layer, with and without interface states at the ZnMgO/CIGS interface. For the case of ideal ZnMgO/CIGS interface, large Mg concentration ($x = 0.36$) necessitates nearly degenerate or degenerate ZnMgO to achieve good efficiency, while at lower Mg concentration ($x = 0.19$) the electron concentration in the ZnMgO is much less critical. The thickness of the ZnMgO layer should also be tailored based on a careful analysis of the total reflection of the incident light. In the presence of non-ideal ZnMgO/CIGS interface, increasing interface trap densities result, as expected, in open-circuit voltage and, consequently, efficiency degradation. Heavy doping of the ZnMgO layer ($n_W \geq 10^{18}$ cm^{-3}) results in full occupation, and inactivation, of the mid-gap traps.

Two-dimensional numerical simulations have finally been used to study the impact of vertical as well as horizontal grain boundaries in the absorber layer of CdTe solar cells. The study considered the effect of absorber doping, grain size, and concentration of Cl_{Te} donor traps at the grain boundaries, a known by-product of recrystallization in the presence of chlorine (a processing step used to increase grain size and yielding more efficient cells). Besides being consistent with known experimental results, such as the increase of efficiency with grain size and absorber acceptor density, our simulations indicate that: *i)* in a columnar absorber (i.e., one where only vertical grain boundaries exist) the presence of Cl_{Te} donor traps at the grain boundaries results in a dip in the band profiles that effectively serves as electron collector, increasing short-circuit current; *ii)* while the same dip acts as a hole barrier and thus can be expected to block holes from flowing through the diode when horizontal grain boundaries are present, under illuminated conditions electron collection at the grain boundary reduces the dip enough to allow substantial hole flow, and the cell's performance is only moderately affected.

In summary, this thesis studied thin-film CIGS and CdTe solar cells using numerical and analytical models with the aim to bring additional knowledge and speed up the progress of thin-film photovoltaics.

This work has been carried out in collaboration with the CNR-IMEM of Parma (Italy), the Physics Department of the University of Parma (Italy), the University of Western Australia and the University of Illinois at Chicago.

Appendix A

Acronyms

AM1.5	Air Mass 1.5
CIGS	$Cu(In,Ga)Se_2$
CNR	Consglio Nazionale delle Ricerche
FF	Fill Factor
GB	Grain Boundary
GI	Grain Interior
IMEM	Istituto dei Materiali per l’Elettronica ed il Magnetismo
SRH	Shockley-Read-Hall (recombination)
TCO	Transparent Conductive Oxide
VBO	Valence Band Offset

Appendix B

List of symbols

χ	electron affinity
E_G	energy gap
N_D	donor doping concetration
N_A	acceptor doping concentration
m_e	electron mass
m_h	hole mass
m_O	vacuum electron mass
μ_e	electron mobility
μ_h	hole mobility
ε	permittivity
ε_0	vacuum pemittivity
J_{SC}	short circuit current density
V_{OC}	open circuit voltage
η	conversion efficiency
DC	direct current
R	recombination
G	optical generation
v_{TH}	thermal velocity
E_F	Fermi energy
Ψ	electrostatic potential
Φ	photon flux
E_C	conduction band energy
E_V	valence band energy

Appendix C

Physical constants

Symbolo	Value	Measurement unit	Name
c	299792458	$\left[\frac{m}{s}\right]$	light speed
h	$6.62606896 \cdot 10^{-34}$	$[Js]$	Planck's constant
π	3.14159265	$[1]$	pi
k	$1.3806503 \cdot 10^{-23}$	$\left[\frac{J}{K}\right]$	Boltzmann's constant
q	$1.60217733 \cdot 10^{-19}$	$[C]$	electron charge
m_e	$9.1093897 \cdot 10^{-31}$	$[kg]$	electron mass
m_p	$1.6726231 \cdot 10^{-27}$	$[kg]$	proton mass
μ_0	$4\pi \cdot 10^{-7}$	$\left[\frac{H}{m}\right]$	vacuum permeability
ε_0	$8.85418781762 \cdot 10^{-12}$	$\left[\frac{F}{m}\right]$	vacuum permittivity
eV	$1.60217733 \cdot 10^{-19}$	$[J]$	electronvolt

Bibliography

[1] B. Dimmler. CIGS and CdTe based thin film PV modules, an industrial r/evolution. *38th Photovoltaic Specialists Conference (PVSC)*, pages 2494–2499, 2012.

[2] I. Repins, M. A. Contreras, B. Egaas, C. DeHart, J. Scharf, C. L. Perkins, B. To, R. Noufi. 19.9%-efficient ZnO/CdS/CuInGaSe_2 solar cell with 81.2% fill factor. *Prog. Photovolt.: Res. Appl.*, 16:235–239, 2008.

[3] J. R. Sites. CdTe cells and modules: Prospects for higher efficiency. *37th Photovoltaic Specialists Conference (PVSC)*, :000136–000139.

[4] M. Burgelman, P. Nollet and S. Degrave. Modelling polycrystalline semiconductor solar cells. *Thin Solid Films*, 361-362:527–532, 2000.

[5] Synopsys®. *Sentaurus Device User Guide*. 2011.

[6] Synopsys®. *Sentaurus Structure Editor User Guide*. 2011.

[7] Charalambos C. Katsidis and Dimitrios I. Siapkas. General Transfer-Matrix Method for Optical Multilayer Systems with Coherent, Partially Coherent, and Incoherent Interference. *Applied Optics*, 41, 2002.

[8] Pochi Yeh. *Optical waves in layered media*. Wiley, 1998.

[9] Antonio Luque, Steven Hegedus. *Handbook of Photovoltaic Science and Engineering*. John Wiley & Sons, 2003. ISBN: 0-471-49196-9.

[10] Luis Castaner, Santiago Silvestre. *Modelling Photovoltaic Systems Using Pspice*. Wiley & Sons Ltd., 2002. ISBN:0470845279.

[11] Mark Lundstrom. ECE 612 Lecture 31: Heterostructure Fundamentals. `www.ecn.purdue.edu/~ee606/downloads/T3.PDF`.

[12] Pochi Yeh. *Optical Waves in Layered Media*. ISBN: 978-0-471-73192-4.

[13] Jaspirit Singh. *Semiconductor Devices: an Introduction*. McGraw-Hill, 1994. ISBN 0-07-113906-0.

[14] W. K. Metzger and M. Gloeckler. The impact of charged grain boundaries on thin-film solar cells and characterization. *J. Appl. Phys.*, 98:063701, 2005.

[15] M. Gloeckler, J. R. Sites, W. K. Metzger. Grain-boundary recombination in Cu(In,Ga)Se_2 solar cells. *J. Appl. Phys.*, 98:113704, 2005.

[16] K. Taretto and U. Rau. Numerical simulation of carrier collection and recombination at grain boundaries in Cu(In,Ga)Se_2 solar cells. *J. Appl. Phys.*, 103:094523, 2008.

[17] U. Rau, K. Taretto, S. Siebentritt. Grain boundaries in Cu(In,Ga)$(Se,S)_2$ thin-film solar cells. *Appl. Phys. A*, 96:221–234, 2009.

[18] C. Persson and A. Zunger. Anomalous grain boundary physics in polycrystalline CuInSe2: the existence of a hole barrier. *Phys. Rev. Lett.*, 91:266401, 2003.

[19] M. J. Hetzer, Y. M. Strzhemechny, M. Gao, M. A. Contreras, A. Zunger, L. J. Brillson. Direct observation of copper depletion and potential changes at copper indium gallium diselenide grain boundaries. *Appl. Phys. Lett.*, 86:162105, 2005.

[20] M. Schmidt, D. Braunger, R. Schaeffer, H. W. Schock, U. Rau. Influence of damp heat on the electrical properties of Cu(In,Ga)Se_2 solar cells. *Thin Solid Films*, 361-362:283–287, 2000.

[21] T.i Minemoto, Y. Hashimoto, T. Satoh, T. Negami, H. Takakura, and Y. Hamakawa. Cu(In,Ga)Se_2 solar cells with controlled conduction band offset of window/Cu(In,Ga)Se_2 layers. *Journal of Applied Physics*, 89:8327–8330, 2000.

[22] J. Marlein, K. Decock, M. Burgelman. Analysis of electrical properties of CIGSSe and Cd-free buffer CIGSSe solar cells. *Thin Solid Films*, 517:2353–2356, 2009.

[23] F.S. Hasoon, X. Li, A. Kanevce, C. Perkins, and S. Asher. Investigation of the Effect of I-ZnO Window Layer on the Device Performance of the Cd-Free CIGS Based Solar Cells. *33rd IEEE Photovoltaic Specialists Conference*, 2008.

[24] X. Li , A. Kanevce , J. V. Li , I. Repins , B. Egaas , and R. Noufi. IMPACT of $Zn_{1-X}Mn_XO$ on Cu(In,Ga)Se_2 THIN-FILM SOLAR CELLS. *34th IEEE Photovoltaic Specialists Conference* , 2008.

[25] T. Minemoto, Y. Hashimoto, W. Shams-Kolahi, T. Satoh, T.i Negami, H. Takakura, Y. Hamakawa. Control of conduction band offset in wide-gap Cu(In,Ga)Se_2 solar cells. *Solar Energy Materials & Solar Cells*, 75:121–126, 2003.

[26] D. J. Cohen, K. C. Ruthe, and S. A. Barnett. Transparent conducting $Zn_{1-x}Mg_xO$:(Al,In) thin films. *Journal of Applied Physics*, 96:459–467, 2004.

[27] T. Minemoto, T. Negami, S. Nishiwaki, H. Takakura, Y. Hamakawa. Preparation of $Zn_{1-x}Mg_xO$ films by radio frequency magnetron sputtering. *Thin Solid Films*, 372:173–176, 2000.

[28] K. Suzuki, H. Shiraki. Evaluation of Surface Recombination Velocity on CdTe Radiation Detectors by Time-of-Flight Measurements. *Nuclear Science*, 56, no. 4:1712–1716, 2009.

[29] A. Romeo, D. L. Bätzner, H. Zogg, A. N. Tiwari. Recrystallization in CdTe/CdS. *Thin Solid Films*, 361-362:420–425, 2000.

[30] S. H. Wei, S. B. Zhang. Theoretical study of doping limits of CdTe. *NCPV Program Review Meeting*, :14–17, 2001.

[31] I. Visoly-Fisher, S. R. Cohen, K. Gartsman, A. Ruzin, D. Cahen. Understanding the Beneficial Role of Grain Boundaries in Polycrystalline Solar Cells from Single Grain Boundary Scanning Probe Microscopy. *Advanced Functional Materials*, 16:649–660, 2006.

[32] S. Smith, P. Zhang, T. Gessert, A. Mascarenhas. Near-field optical beam-induced currents in CdTe/CdS solar cells: Direct measurement of enhanced photoresponse at grain boundaries. *Appl. Phys. Lett.85*, 17:3854–3856, 2004.

[33] E. Colegrove, R. Banai, C. Blissett, C. Buurma, J. Ellsworth, M. Morley, S. Barnes, C. Gilmore, J. D. Bergeson, R. Dhere, M. Scott, T. Gessert, Siva Sivananthan. High-Efficiency Polycrystalline CdS/CdTe Solar Cells on Buffered Commercial TCO-Coated Glass. *Journal of Electronic Materials*, 41, 10:2833–2837, 2012.

[34] N. R. Paudel, K. A. Wieland, A. D. Compaan. High Efficiency Sputtered CdS/CdTe Cells without CdCl2 Activation. *Mater. Res. Soc. Symp. Proc.*, 1323:139–144, 2011.

Acknowledgements

There are many people I would like to acknowledge for their contribution to my PhD. I will try to thank anyone of them not in order of importance but in chronological order. I start with my gratitude to my parents, for all their support. I thank my adviser Roberto Menozzi for his precious guidance, the possibility to organize two wonderful leaves, his time and availability. I thank Carlo Concari for giving me the possibility of my first overseas conference. Thanks to all of my professors and colleagues at the University and at CNR-IMEM of Parma for improving my knowledge and for their time. Thanks to my friends. I thank Lorenzo Faraone (Laurie) for giving me the opportunity of being part of his research group and for inviting me to many events and celebrations; thanks to his father for the best *pasta e fagioli*. Thanks Sabine Betts for your unique support in organizing my leave in Australia. I thank Lyn and Rob D'Agostino for hosting me in their family. Thanks to all of my Aussie colleagues and mates. Thanks to Siva Sivanantham for inviting me at UIC, for all the meetings and events, for the opportunity to visit his laboratories. Thanks Yesim Anter for your unique support in organizing my leave in the U.S.. Thanks to all of my colleagues and friends in the States.